EXPERIMENTAL AND NUMERICAL INVESTIGATION OF FLOW FIELD AROUND FLAPPING AIRFOILS MAKING FIGURE-OF-EIGHT IN HOVER

A THESIS SUBMITTED TO
THE GRADUATE SCHOOL OF NATURAL AND APPLIED SCIENCES
OF
MIDDLE EAST TECHNICAL UNIVERSITY

BY

ÖZGE BAŞKAN

IN PARTIAL FULFILLEMENT OF THE REQUIREMENTS
FOR
THE DEGREE OF MASTER OF SCIENCE
IN
AEROSPACE ENGINEERING

SEPTEMBER 2009

Approval of the thesis:

EXPERIMENTAL AND NUMERICAL INVESTIGATION OF FLOW FIELD AROUND FLAPPING AIRFOILS MAKING FIGURE-OF-EIGHT IN HOVER

Submitted by ÖZGE BAŞKAN in partial fulfillment of the requirements for the degree of **Master of Science in Aerospace Engineering Department, Middle East Technical University** by,

Prof. Dr. Canan Özgen
Dean, Graduate School of **Natural and Applied Sciences** ____________________

Prof. Dr. İsmail H. Tuncer
Head of Department, **Aerospace Engineering** ____________________

Prof. Dr. H. Nafiz Alemdaroğlu
Supervisor, **Aerospace Engineering Dept., METU** ____________________

Examining Committee Members:

Prof. Dr. Yusuf Özyörük ____________________
Aerospace Engineering Dept., METU

Prof. Dr. H. Nafiz Alemdaroğlu ____________________
Aerospace Engineering Dept., METU

Prof. Dr. Kahraman Albayrak ____________________
Mechanical Engineering Dept., METU

Assoc. Prof. Dr. Serkan Özgen ____________________
Aerospace Engineering Dept., METU

Dr. Ebru Ortakaya ____________________
The Scientific & Technological Research
Council of Turkey (TÜBİTAK-SAGE)

Date: 11 / 09 / 2009

I hereby declare that all information in this document has been obtained and presented in accordance with academic rules and ethical conduct. I also declare that, as required by these rules and conduct, I have fully cited and referenced all material and results that are not original to this work.

Name, Last name: ÖZGE BAŞKAN

Signature :

ABSTRACT

EXPERIMENTAL AND NUMERICAL INVESTIGATION OF FLOW FIELD AROUND FLAPPING AIRFOILS MAKING FIGURE-OF-EIGHT IN HOVER

BAŞKAN, Özge
M.Sc., Department of Aerospace Engineering
Supervisor: Prof. Dr. H. Nafiz Alemdaroğlu

September 2009, 94 pages

The aim of this study is to investigate the flow field around a flapping airfoil making figure-of-eight motion in hover and to compare these results with those of linear flapping motion. Aerodynamic characteristics of these two-dimensional flapping motions are analyzed in incompressible, laminar flow at very low Reynolds numbers regime using both the numerical (Computational Fluid Dynamics, CFD) and the experimental (Particle Image Velocimetry, PIV) tools. Numerical analyses are performed to investigate the effect of different parameters such as the amplitude of motion in y-direction, angle of attack, Reynolds number and camber on the aerodynamic force coefficients and vortex formation mechanisms. Both symmetric and cambered airfoil sections are investigated at three different starting angles of attack for five different amplitudes of motion in y-direction including linear flapping motion. Experimental simulations are performed in order to verify the numerical results only for linear motion at Reynolds number of 1000 for symmetric and cambered airfoils at three different angles of attack. Computed vortical structures are then compared to vorticity contours obtained from the experiments and advantages of figure-of–eight motion over linear motion are discussed.

Keywords: Flapping Motion, Unsteady Aerodynamics, CFD, PIV

ÖZ

HAVADA ASILI KONUMDA SEKİZ ŞEKLİ ÇİZEREK ÇIRPAN KANAT PROFİLLERİNİN ETRAFINDAKİ AKIŞ ALANININ SAYISAL VE DENEYSEL OLARAK İNCELENMESİ

BAŞKAN, Özge
Yüksek Lisans, Havacılık ve Uzay Mühendisliği Bölümü
Tez Yöneticisi: Prof. Dr. H. Nafiz Alemdaroğlu

Eylül 2009, 94 sayfa

Bu çalışmanın amacı havada asılı durumda sekiz şekli üzerinde hareket eden çırpan kanat profili etrafındaki akış alanını incelemek ve bu hareketin sonuçları ile farklı bir havada kalma durumu olan çizgisel hareketin sonuçlarını karşılaştırmaktır. İki boyutlu bu modların aerodinamik özellikleri düşük Reynolds sayısında sıkıştırılamaz laminar akış içinde hem sayısal (Hesaplamalı Akışkanlar Dinamiği, HAD) hem de deneysel yöntemler (Parçacık Görüntüleme ile Hız Ölçümü, PGHÖ) kullanılarak analiz edilmiştir. Sayısal analizler y yönündeki hareket genliği, hücum açısı, Reynolds sayısı ve kamburluklu gibi farklı parametrelerin aerodinamik kuvvet katsayıları ve girdap oluşum mekanizmalarının üzerindeki etkisini incelemek için gerçekleştirilmiştir. Simetrik ve kamburluklu kanat profilleri üç farklı başlangıç hücum açısında çizgisel çırpma hareketini de içeren y yönündeki beş farklı hareket genliği için incelenmiştir. Deneysel çalışmalar sayısal çözümleri doğrulamak için Reynolds sayısı 1000'de simetrik ve kamburluklu kanat profilleri kullanılarak üç farklı hücum açısında sadece çizgisel kanat çırpma hareketi için gerçekleştirilmiştir. Hesaplanan girdap yapıları deneysel çalışmlardan elde edilen girdap eşeğrileri ile karşılaştırılmıştır ve sekiz şekli üzerinde gerçekleşen hareketin çizgisel harekete göre avantajları ortaya çıkarılmıştır.

Anahtar Kelimeler: Çırpan Kanat Hareketi, Zamana Bağlı Aerodinamik, CFD, PIV

To My Parents Gülay and Hüseyin Başkan and To My Sister Elif…

ACKNOWLEDGEMENTS

I wish to state my sincere thanks to my supervisor Prof. Dr. H. Nafiz Alemdaroğlu for his support, advice, guidance and criticism during this thesis.

I would like to thank to Mr. Murat Ceylan for his kind contribution throughout the experimental part of the study.

I would like to extend my thanks to Yaroslav Novikov for his assistance.

I would like to thank to my friends Aslı, Ceren, Gökçen, Merve, Remziye and many others for always believing in me and supporting me in any case. Their endless encouragement made it possible to complete this study.

I would like to express my special thanks to Mustafa Perçin, without whom I have never made it this far and with whom I wish to carry on the path of life.

Finally, I would like to express my eternal gratitude to my family. It makes me feel better to know how much they love me.

TABLE OF CONTENTS

CHAPTERS

LIST OF TABLES

LIST OF FIGURES

LIST OF SYMBOLS

a	axis of rotation (=0 at leading edge and =1 at trailing edge)
A	amplitude in x-direction
B	amplitude in y-direction
C_H	horizontal force coefficient
C_V	vertical force coefficient
c	chord
LEV	leading edge vortex
$\bar{H}$	average horizontal force
TEV	trailing edge vortex
MAV	Micro Air Vehicle
Re	Reynolds number
t	time
t_a	time corresponding to the xa location where the angle of attack changes
t_v	time corresponding to the xv location where the velocity changes
T	period
$\bar{V}$	average vertical force
V	velocity of the flapping motion
V_0	maximum velocity during the flapping motion
x_a	x position at the beginning of angle of attack change
x_v	x position at the end of constant velocity region
$x_{T/4}$	maximum x location, half-amplitude
α	angle of attack
α_0	initial angle of attack
I	unit tensor
μ	dynamic viscosity
ρ	density
τ	stress tensor
ν	kinematic viscosity
ω	vorticity, angular velocity of the flapping motion

CHAPTER 1

INTRODUCTION

1.1 General Introduction

Miniature flying aircrafts known as Micro Air Vehicles (MAVs) consisting of components less than 15 cm in size (a definition employed by Defense Advanced Research Project Agency, DARPA) have gained a remarkable interest in recent years. Modern military and civilian needs have caused a demand for small, highly maneuverable vehicles that can perform a wide range of tasks. These vehicles can be used for surveillance and reconnaissance, as well as biochemical sensing at remote, telecommunications, crop monitoring, mineral exploration and coast-watch.

Small scale conventional fixed-wing and rotorcraft vehicles are restricted in design due to aerodynamic constraints. At low Reynolds numbers (10^1~10^5) airfoil characteristics have limitations imposed by the dominance of viscous forces which cause an increase in boundary layer thickness and viscous drag. Relatively small kinetic energy of the fluid elements results in flow separation from the surface of the wing thereby increasing pressure drag and loss of lift. Although rotary-wing designs have proven to easily remain in hover and maneuver in any direction, they cannot attain long endurance.

Nature provides an excellent vehicle model for birds and insects which make use of the flapping wings to produce simultaneously the necessary thrust for forward motion and continuous lift to keep them flying. This is a completely different picture from what we see in aircraft motion in which lift is created by fixed wings to ensure attached and steady flow, while natural fliers use unsteady aerodynamics by flapping their wings to create vortices shed (separated) from both the leading and the trailing edges of the wings. The resulting low pressure regions give raise to relatively high instantaneous lift and thrust forces when compared to fixed wings [1].

High maneuverability and hovering capabilities of birds and insects attracted high attention and promoted the investigation of the aerodynamics of flapping wing motion. Biologists have described the kinematics of flapping wing motion and suggested empirical correlations between flight characteristics of many different families of birds and insects. Biofluiddynamicists have conducted a series of studies to explain the underlying physical phenomena in both the quasi-steady theory and fully unsteady regime.

The fundamental physics of unsteady flapping wings can be explained by simplified two-dimensional experiments, and further supported by theoretical or numerical models and solutions. Wang [2] showed that two-dimensional computation of flapping motion is a reliable tool and a useful reference point to approximate the three dimensional motion. Most of the studies in the related literature implement a two-dimensional approach to capture the basic characteristics of flapping motion in detail. These studies conducted for unsteady, laminar, incompressible flow at low Reynolds number (10^1–10^5) simulate the same environment as for the similarly sized biological fliers.

The aim of this thesis is to analyze the flow field around flapping airfoils making the figure-of-eight in hover. Two types of flapping motion (linear and figure-of-eight motion) kinematics are investigated during this study. The second type of motion is based on the linear study prescribed by Kurtuluş et al. [3], and is extended to the analysis of airfoil profiles moving on a different trajectory, i.e. figure-of–eight, which in addition to linear motion includes the motion in the perpendicular direction (i.e. in y-direction). To ensure the continuity of the path followed by the airfoils, Lissajous curves are used. Analysis is performed to assess the importance of motion in y-direction on the aerodynamic force coefficients and vortex formation mechanisms. The aerodynamic force coefficients are then compared for two different airfoil profiles (symmetric and cambered), different Reynolds numbers and angles of attack [4]. Vorticity plots are also included and discussed.

This thesis comprises two parts in terms of the techniques used for the analysis, i.e. numerical and experimental studies. Both studies are performed for two airfoil profiles (NACA 0012 and NACA 6412), three different angles of attack (30˚, 45˚ and 60˚) at Reynolds numbers of 200, 1000 and 5000. Numerical study is based on unsteady, laminar and incompressible fluid characteristics solved for flow field around two-dimensional airfoils during the flapping motion with a commercially available Computational Fluid

Dynamics (CFD) code, FLUENT. Two dimensional Navier-Stokes equations are solved by using the moving grid technique. After grid refinement procedures, O-type grids are generated around the profiles with grid outer boundaries chosen to be at 15 chord lengths. Experimental studies are performed using the Particle Imaging Velocimetry (PIV) technique to assess the computational accuracy of the numerical solutions. Numerical and experimental studies are then compared in terms of vorticity created in the flow field.

1.2 Definition of Motion

In general, wing stroke of an insect or a bird in hover is investigated in four main phases: two translational phases (upstroke and downstroke) where the translation of wings occur at high angles of attack and two rotational phases (pronation and supination) where the direction of motion of the wings is reversed.

In the study conducted by Kurtuluş [3] the flapping motion is divided into 4 distinct regions. The first region corresponds to half of the downstroke while the second one corresponds to half of the upstroke. The third and fourth regions are the mirror images of these two regions, corresponding to the second half of upstroke and downstroke, respectively. Figure 1.1 shows the detailed description of the flapping motion for one period.

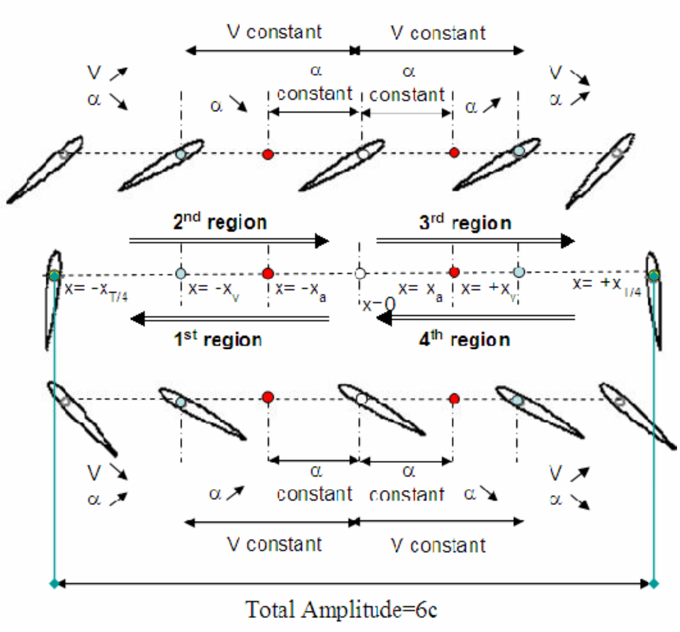

Figure 1.1 Definition of flapping motion prescribed by Kurtuluş [3]

Each region is composed of a translational phase and a rotational phase. In the translational phase, the airfoil translates with a constant velocity until the time t_v and position x_v, at which the velocity starts to decrease. A rotational motion around a point on the chord line (1/4c, 1/2c, 3/4c for 3 different cases) from leading edge is superimposed on the translational motion at a predefined time t_a and position x_a. Each stroke starts from rest and comes to a stop.

T is the period of the flapping motion. From the origin (x=0) until the position x_v at time t_v the airfoil moves with a constant velocity. During the time interval $[t_v, T/4]$ the airfoil decelerates and the velocity becomes zero at the quarter period meanwhile at time t_a and position x_a, the airfoil also starts to rotate around the center of rotation where it reaches 90° angle of attack at t=T/4.

Velocity V and the angular velocity variation ω prescribed by Kurtuluş [3] are given in Equation 1.1 and Equation 1.2 respectively. Kurtuluş [3] states that this type of motion is chosen to ensure the continuity of the velocities and the accelerations between the two phases of the translational motion.

$$V = V_0 \cos\left(\frac{\pi}{2}\frac{(t - t_v)}{\left(\frac{T}{4} - t_v\right)}\right) \tag{1.1}$$

$$\omega = -\frac{\omega_{\max}}{2}\left(1 - \cos\left(\frac{\pi(t - t_a)}{\frac{T}{4} - t_a}\right)\right) \tag{1.2}$$

where

$$\omega_{\max} = \frac{2\alpha_0}{\frac{T}{4} - t_a} \tag{1.3}$$

$$T = \frac{4\pi}{2|V_0|}\left(x_{T/4} - x_v\right) + t_v \tag{1.4}$$

Specifics of current study regarding the linear flapping motion are the same as that of Kurtuluş. For all cases studied, $x_v = x_c = 2c$ and $t_v = t_c$ and the rotation occurs at quarter chord (1/4 c) from the LE.

The second type of motion is superposition of this kinematics and a motion in the y-direction and is called as the "Figure-of-eight motion". In this type of motion the airfoil moves on a continuous trajectory defined by Lissajous curves which is the graph of a system of parametric equations describing a complex harmonic motion. The equation system is given as follows:

$$x = A\sin(at + \delta) \tag{1.5}$$

$$y = B\sin(bt) \tag{1.6}$$

where

$$t \in [0,2\pi]$$

$\delta = \frac{\pi}{2}$, $a = 1$ and $b = 2$ values correspond to the horizontal figure-of-eight shown in Figure 1.2.

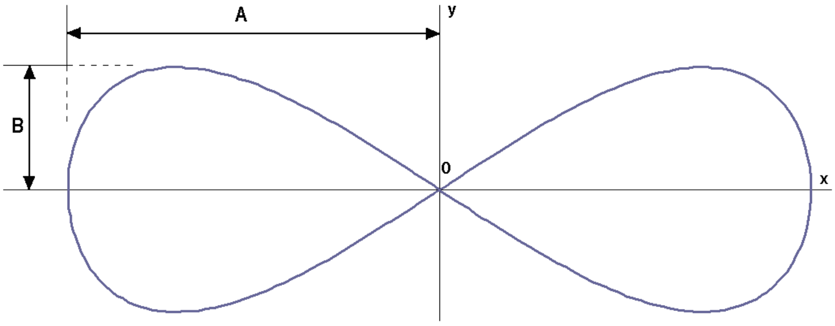

Figure 1.2 Lissajous curve used for figure-of-eight motion

This system of equations (Equation 1.5 and Equation 1.6) are adapted for the figure-of-eight motion used in this thesis. When the figure-of-eight motion is examined in x and in y directions, motion in the x-direction is the same as the linear motion. Kinematics of the motion in y-direction is established by horizontal figure-of-eight, i.e. position of the airfoil on the x axis is determined by linear motion whereas its corresponding position on the y axis is determined by the system of equations given by the Lissajous curves. Figure 1.3 shows the positions of the wing on the Lissajous curve.

For numerical analysis of the figure-of-eight motion five different B values (amplitude in y-direction) have been analyzed to determine the effect of the motion in y-direction (for the case when B is equal to zero, the kinematics of the motion is the same as the linear flapping motion studied by Kurtuluş [3] and Sarıgöl [4]). Total displacement of the airfoil is 6 chord lengths in horizontal direction. A is the half of this displacement and corresponds to 3c for all cases studied. Analysis of camber effect on the aerodynamics of the motion is studied using the two different airfoil profiles (NACA 0012 and NACA 6412); effects of parameters such as angle of attack and Reynolds number are also investigated.

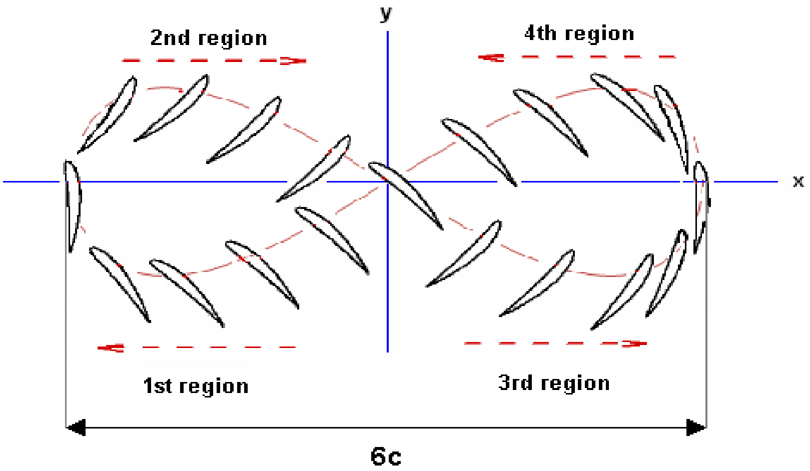

Figure 1.3 Positions of the wing on Lissajous curve

1.3 Objective and Outline of the Present Study

This thesis is aimed at identifying and understanding the underlying mechanisms that are responsible for the generation of aerodynamic forces in flapping motion making figure-of-eight in hover and analyzing the advantages of this motion over linear flapping motion. The numerical studies are extended to cover linear and figure-of-eight motions at different Reynolds numbers and angle of attack values for symmetric and cambered airfoil profiles. The time dependent vorticity contours of the linear flapping motion by using PIV. Numerical and experimental results of linear flapping motion are thereafter compared with each other qualitatively and the flow fields are investigated for vortex regions.

The present study is organized in 6 chapters. Chapter 1 reviews the kinematics of linear flapping motion equations of which are prescribed by Kurtuluş [3] and the figure-of-eight motion comprising the motion in y-direction. Brief information about the applications of Micro Air Vehicles and the scope and the outline of the present study are also given in this chapter.

The second chapter, Chapter 2, reviews the previous studies conducted by several researchers.

The numerical and experimental setups used in the study are described in Chapter 3. The properties of the solver and the grid are described and the selection of grid size and time step are explained clearly. The experimental analysis is conducted using PIV technique and the principles of this technique are given in this chapter.

In Chapter 4, two-dimensional numerical simulations of linear and figure-of-eight flapping motion analysis are presented. The numerical simulations are carried out using commercially available CFD code, Fluent. Different parameters are concerned during the simulation of two-dimensional flapping motion but the study concerns mainly about the effect of motion in y-direction. Effect of initial angle of attack is studied on both symmetrical and cambered NACA airfoils having the same maximum thickness at different Reynolds number values. The aerodynamic force coefficient variations are compared with each other. The vortex regions of these profiles are investigated at different angle of attack.

Chapter 5 presents the two-dimensional experimental investigation of linear flapping motion carried out for both symmetrical the cambered airfoil profiles. The experiments are carried out for a Reynolds number of 1000 and for three different angles of attack. The experimental results are then compared to those obtained from the numerical solutions of linear flapping motion.

The last chapter, Chapter 6 is dedicated to conclusions of the study. Some ideas for the future studies are also given in this last chapter.

CHAPTER 2

LITERATURE SURVEY

Investigations on a number of natural and manmade flyers have increased due to the interest in Micro Air Vehicles (MAVs). Birds and insects have attracted the attention of biologists for many years, and active studies in the aerospace engineering community have been conducted to understand the underlying physical aspects of both lift and thrust creating mechanisms. Substantial literature exists, especially in the biological community. Although some of the studies discuss flying primarily from the analytical point of view general references offer broad accounts of biological flight, including geometric scaling laws, power and morphology as well as simplified modeling.

Analytical models based on quasi-steady theory were used as a first estimate of the forces acting on flapping wings, but these studies failed since the flow induced by the motion of bird and insect wings are highly unsteady and vortical as shown first by Weis-Fogh & Jensen [5] using tethered locusts. The developed quasi-steady approach was revised by Sane & Dickinson [6], which included some rotational effects but even then the results remained uncertain. Afterwards, no much effort has been made to obtain a more accurate analytical model for the aerodynamic forces.

Ellington [7-12] highlighted important physical characteristics in the study of hovering insects in the series of papers and explained many of the key principles involved in flapping wing aerodynamics. These papers illustrate some crucial factors regarding the nature of the aerodynamics of flapping wings. In addition to this, useful accounts of flapping kinematics and power expenditure contribute to the general understanding of the subject with a well documented comparison between analytical techniques and experimental data. The results revealed that the aerodynamics of hovering animals does not rely on quasi-steady approach but it is based on rotational lift mechanisms instead.

When it was well understood that rotational structures highly affect the flow characteristics around flapping wings, experiments and numerical simulations for biological flight and simplified modeling were conducted. Biological studies were performed based on the real flight characteristics of the birds and insects. Besides, in the simplified modeling studies, different airfoil profiles were used instead of the real insect/bird wing geometries and mostly based on the aerodynamics.

To study biological flight, robotic models are used to study flapping wing flight [robotic studies]. With geometric and kinematic similarities, the dynamic similarity is maintained by scaling up the wing dimension while appropriately lowering the flapping frequency, rendering the Reynolds number or the reduced frequency unchanged [13].

Dickinson and Götz [14] used a robotic model to fill the deficit in low Reynolds number regime by quantifying the time-dependence of aerodynamic forces for a simple motion, rapid acceleration from rest to a constant velocity at a fixed angle of attack. The study combined the measurement of lift and drags on a two-dimensional model with simultaneous flow visualization and aimed at the characterization of time-dependency of the forces produced by impulsively started wings. The results indicated the contribution of the unsteady process of vortex generation at large angles of attack to the production of aerodynamic forces in insect flight and appropriateness of the complex dynamic behavior of impulsively started wing profiles for models of insect flight than are steady-state approximations.

Ellington et al. [15] visualized the flow over the wings of a hovering *Hawkmoth Manduca sexta* (Figure 2.1) and a large mechanical model–the flapper. They discovered that an intense leading edge vortex (LEV) spiral out toward the wingtip. Their finding provided a qualitative explanation of one particular high-lift mechanism.

Figure 2.1 Manduca sexta [16]

Van den Berg and Ellington [17]-[18] studied a three dimensional flow visualization of a hovering *hawkmoth*. The details of this flow pattern were studied with a scaled-up, robotic insect (the flapper) that accurately mimicked the wing movements of a hovering *hawkmoth*. Smoke released from the leading edge of the flapper wing confirmed the existence of a small, strong and stable leading-edge vortex, increasing in size from wingbase to wingtip. They also showed that the leading-edge vortex have a strong axial flow velocity which stabilizes it and reduces its diameter and the vortex separated from the wing at approximately 75% of the wing length and thus feeds vorticity into a large, tangled tip vortex.

Dickinson et al. [19] also used a robotic model, representing a fruit fly, to directly measure forces and visualize the flow patterns on a robot fly at low Reynolds number regime covering a range of Reynolds number from 8 to 500. A tank filled with mineral oil was used in the experiments to match the experimental Reynolds number to that of a typical *Drosophila* (Figure 2.2), Re=136. They demonstrated two force peaks at the rotation phase, namely, the rotational mechanism associated with fast pitch-up, and the wake-capture mechanism resulting from the airfoil and vortical flow interactions.

Figure 2.2 Drosophila [20]

Birch and Dickinson [21] further observed substantially different flow patterns around the model used in [19], based on large moths and small flies, to investigate the impact of the scaling parameters on the aerodynamic forces. They used two-dimensional Digital Particle Image Velocimetry (DPIV) to visualize flow patterns around the flapping wing of a dynamically scaled model insect for a series of reciprocating strokes starting from rest and the pattern of fluid motion was directly compared with the time history of force production. They reported that at low Reynolds numbers, flapping wings do not generate a spiral vortex similar to that produced by delta-wing aircraft. They also found that limiting spanwise flow with fences and edge baffles does not cause detachment of the leading edge vortex. The data supported that downward flow induced by tip vortices limits the growth of the leading-edge vortex.

Usherwood et al. [22] conducted a study on flapping *hawkmoth* models which demonstrates the importance of a spiral leading-edge vortex created by dynamic stall, and maintained by some aspect of spanwise flow, for creating the lift required during flight. They also investigated that steadily revolving model hawkmoth wings produce high vertical (lift) and horizontal (profile drag) force coefficients because of the presence of a leading-edge vortex. Results for bumblebee and hawkmoth wings agreed with those published previously for *Drosophila* (Re~200).

Sane and Dickinson [6] used a dynamically scaled model insect to measure the rotational forces produced by a flapping insect wing. A steadily translating wing was rotated at a range of constant angular velocities, and the resulting aerodynamic forces were measured using a sensor attached to the base of the wing. These instantaneous forces were compared with quasi-steady estimates based on translational force coefficients. The results revealed the effect of wing rotation on the production of aerodynamic forces by a flapping airfoil and the agreement of the measured rotational force coefficients with the theoretically estimated values. Translation-based models of insect flight revised by incorporating wing rotation was compared with traditional models, but the revised model showed better agreement with the time course of aerodynamic force generation over a large variety of kinematic patterns.

Birch et al. [23] quantified both the forces and fluid motion around an insect wing flapping at *Re*=120 and *Re*=1400 for 45° angle of attack. They used a dynamically scaled robot and DPIV. The results showed that the transport of vorticity from the leading edge to the wake that permits prolonged vortex attachment takes different forms at different Re and stability of forces and flow reaches different equilibrium points, as measured by net force and circulation, and is generated by qualitatively different flows.

Lehmann et al. [24] utilized a dynamically scaled mechanical model of the small fruit fly *Drosophila melanogaster* in low Reynolds number regime (between 100–200) to investigate the effect of contralateral wing interactions during stroke reversal (the clap-and-fling) on force enhancement. DPIV technique was used to analyze clap-and-fling mechanism and it was shown that the most obvious effect of the bilateral image wing on flow occurs during the early phase of the fling, due to a strong fluid influx between the wings as they separate.

In the study conducted by Lu et al. [25], the first physical images revealing the integral flow structures and their evolutions of *dragonfly* (Figure 2.3) hovering are presented, based on the dye flow visualization conducted on an electromechanical model in water tunnel. Together with the quantitative information derived from the images, they obtained that spanwise flow is conspicuous regardless of the large aspect ratio of the wing and the leading-edge vortex contains dual-vortex structure: the primary vortex do not develop along the leading edge but moves inboard, leaving a space for the formation of a same-sense minor vortex outside the primary vortex. They also found that the development of the leading-edge vortex shows a delay with respect to the translational motion of the wing and in most cases with forewing–hindwing interaction; the interaction is generally detrimental to the leading-edge vortices and is attenuated with the increase of the wing-root spacing.

Figure 2.3 Dragonfly [26]

In addition to robotic models, measurements for real flyers were also conducted. Dickinson et al. [27] introduced a previously unknown component to the turning response of *Drosophila*: modulation of ventral-flip timing, which occurs during the transition from downstroke to upstroke. The results raised issues at both the aerodynamic and neurobiological levels. They explained the independent control of flip timing and wing-beat amplitude by direct flight musculature responsible for steering movements and the interaction of these behaviors in production of aerodynamic forces.

High-speed videography was used in the study conducted by Willmott and Ellington [28] to record sequences of individual hawkmoths in free flight over a range of speeds from hovering to 5 m/s. The following paper of Willmott and Ellington [29] explained the calculation of mean lift coefficients for *hawkmoth* flight at a range of speeds in order to investigate the aerodynamic significance of kinematic variation which accompanies changes in forward velocity. The investigation revealed the importance of new techniques which can accurately simulate both the flow around the wings and the instantaneous forces and full investigation of the impact of structures such as leading-edge vortices.

Srygley and Thomas [30] reported a study on the force generation mechanisms of free-flying butterflies by using high-speed, smoke-wire flow visualizations to obtain qualitative images of the airflow around flapping wings. They observed clear evidence of LEV structures. In comparison, in moth and fly flight, the helical structure and the spanwise, axial flow patterns appear to be much weaker. They suggested that free-flying butterflies use a variety of aerodynamic mechanisms to generate force, including wake capture, LEVs, active and inactive upstrokes, rapid rotation, and clap-and-fling; these different mechanisms are often used in successive strokes as seen during take-off, maneuvering, maintaining steady flight, and landing.

Further refining the experimental techniques, Fry et al. [31] used a 3D infrared high-speed video to capture the wing and body kinematics of free-flying fruit flies, *Drosophila melanogaster*, performing rapid flight maneuvers, and replayed them on their robotic model to measure the aerodynamic forces produced by the wings and the instantaneous forces, torques and power for a detailed analysis of hovering aerodynamics were estimated directly. They reported that the fly generates sufficient torque for rapid turn with subtle modifications in wing motion, and suggested that inertia, not viscous forces, dominate the flight dynamics of flies.

Bomphrey et al. [32] presented the first DPIV analysis of the flow field around the flapping wings of an insect (the tobacco *hawkmoth Manduca sexta*). Detailed DPIV measurements and smoke visualizations showed that a LEV is present above the wings towards the end of the downstroke, as the net upward force peaks and the structure of LEV is consistent with that recently reported in free-flying butterflies and dragonflies: the LEV is continuous across the thorax and runs along each wing to the wingtip, where it inflects to form the wingtip trailing vortices.

Warrick et al. [33] measured the wake of hovering rufous hummingbirds (*Selasphorus rufus*) (Figure 2.4) by using DPIV. Results showed that there exists force asymmetry: hummingbirds produce 75% of their weight support during the downstroke and only 25% during the upstroke. They reported inversion of the cambered wings during the upstroke, as well as evidence of LEVs, created during the downstroke. As suggested by the Reynolds number, a hummingbird’s aerodynamics regime overlaps that of larger insects.

Figure 2.4 Selasphorus rufus [34]

There exist many numerical studies covering a very wide range of parameters investigating the flapping wing motion of real fliers. Ramamurti and Sandberg [35] employed a finite element flow solver to compute unsteady flow past a three-dimensional *Drosophila* wing undergoing flapping motion. The computed thrust and drag forces were compared to the results of previous experimental studies. Grid-refinement study was also conducted to validate the computational results, and a grid-independent solution was achieved. The same solver was utilized to solve the viscous flow past a NACA 0012 airfoil at various pitching frequencies. The thrust generating mechanism of a flapping foil undergoing pitching and heaving motions at very low Reynolds number was also investigated. Results showed that, high thrust forces are achieved when the wing rotation is advanced with respect to the stroke reversal. They also observed that the combined translational and rotational mechanisms are necessary to describe accurately the force time histories and unsteady aerodynamics of flapping wing.

Sun and Tang [36] studied the lift and power requirements for hovering flight in *Drosophila virilis* using the computational fluid dynamics method. They numerically obtained the velocity and pressure fields, and calculated the aerodynamic forces and moments. On the basis of the aerodynamic forces, moments and the inertial torques, the lift and power requirements for hovering flight were acquired. The results showed that the energy expended for a given mean lift in advanced rotation and delayed rotation cases is much larger than that in the case of symmetrical rotation. They also commented that symmetrical rotation is employed by the insect for balanced, long-duration flight and advanced rotation and delayed rotation is employed for maneuvering.

Miller and Peskin [37]-[38] used the immersed boundary method to solve the two-dimensional Navier–Stokes equations for two immersed wings performing an idealized 'clap and fling' stroke and a 'fling' half-stroke. Lift coefficients were calculated as functions of time per wing for a range of Reynolds numbers between 8 and 128. The instantaneous streamlines around each wing throughout the stroke cycle were calculated and the changes in lift were related to the relative strengths and positions of the leading and trailing edge vortices. The results showed that lift generation per wing during the 'clap and fling' of two wings when compared to the average lift produced by one wing with the same motion falls into two distinct patterns. Their results suggested that the Weis-Fogh mechanism of lift generation have greater benefit to insects flight at lower Re. Drag coefficients calculated during fling were also substantially higher for the two-winged case than the one-winged case, particularly at lower Re.

Wu and Sun [39] investigated the unsteady aerodynamic forces of a model fruit fly wing in flapping motion by numerically solving the Navier-Stokes equations. They showed that the forces depend on five non-dimensional parameters such as; Reynolds number, stroke amplitude, mid-stroke angle, non-dimensional duration of wing rotation and rotation timing. This study also revealed that the delayed stall mechanism results in large aerodynamic coefficients.

A multi-block and overset grid-based CFD study was conducted by Aono and Liu [40] for the unsteady flows about a realistic body-wing model and the force-generation in the flapping flight of the *hawkmoth* hovering. In computations, the geometric-and-kinematic model was constructed based on the experimental data of a real *hawkmoth*. The results demonstrated the presence of interaction among the leading-edge vortex (LEV), the trailing-edge vortex (TEV) and the wing tip vortex (TV), and hence quantified the roles of these vortices in aerodynamic force-generation.

Zuo et al. [41] conducted a computational fluid dynamics analysis to study the unsteady aerodynamics of a virtual flying bumblebee during hovering flight. The analysis established an overall understanding of the viscous and unsteady flow around the virtual flying *bumblebee* (Figure 2.5) and of the time course of instantaneous force production, which reveals that hovering flight is dominated by the unsteady aerodynamics of both the instantaneous dynamics and also the past history of the wing.

Figure 2.5 Bumblebee [42]

Aerodynamic force generation in hovering flight in a tiny insect, *Encarsia Formosa* (Figure 2.6), was covered in the study conducted by Sun and Yu [43]. The Navier-Stokes equations were solved over moving overset grids. It was found out that the fling produces a large lift peak at the beginning of the downstroke whereas the clap produces a large lift peak near the end of the subsequent upstroke. The calculated mean lift was enough to support the weight of the insect.

Figure 2.6 Encarsia Formosa [44]

Bos et al. [45] investigated the influence of different wing kinematic models on the aerodynamic performance of a hovering insect by means of two-dimensional time dependent Navier-Stokes simulations. They considered a harmonic model, a Robofly model and two more realistic fruity models, all dynamically scaled at Re = 110. They had studied the vortex dynamics in detail as well as the resulting lift and drag forces. The results revealed that there are significant differences between the forces resulting from simplified wing kinematics and actual fruit fly wing kinematic models. In addition, the flow simulation results shed light on the effect of different characteristic features of the insect wing motion. The angle of attack variation used by real fruit flies increases aerodynamic performance, whereas the deviation is most likely used for leveling the forces over the cycle.

There are some biological comparative studies available in the literature used mainly to validate the numerical studies. In the study conducted by Liu [46] a new paradigm of the so-called, *simulation-based biological fluid dynamics* that can digitize and visualize swimming and flying by using computational mechanical modeling of the biological fluid dynamics through faithful reconstruction of morphology and realistic representation of kinematics of an individual object was proposed. The paradigm is an integrated computational system, involving a morphological modeling subsystem, a kinematic modeling subsystem, a CFD modeling subsystem, and a post-processing subsystem for visualization. The method was tested on a realistic moth’s model and noticed an overall understanding of the complicated vortex structures around a 3D flapping wing during the complete cycle of translational and rotational motions, as well as the corresponding time course of instantaneous force-production.

Wang et al. [47] compared computational, experimental and quasi-steady forces in a generic hovering wing undergoing sinusoidal motion along a horizontal stroke plane using DPIV technique. They investigated unsteady effects and compared two-dimensional computations and three-dimensional experiments in several qualitatively different kinematic patterns. They noted that the steady state two-dimensional forces underestimate the three-dimensional forces whereas the transient two-dimensional forces are much closer to the actual three-dimensional forces.

The simplified configurations are mostly the studies based on the aerodynamic aspects. The models are simplified such that different airfoil profiles are used instead of the real insect/bird wing geometries. Two-dimensional resolved computation of insect hovering studied by Wang [48]-[49] explained that a two-dimensional hovering motion can generate enough lift to support a typical insect weight and suggests that three-dimensionality is not essential for hovering. In this study, Navier-Stokes equations were solved in elliptical coordinates for an elliptical wing to quantify the vortex dynamics that is essential for hovering and to identify a minimum two dimensional model that produces sufficient lift. The vortex dynamics further elucidates the role of the phase relation between the wing translation and rotation in lift generation. It also explained that the instantaneous forces can reach a periodic state after only a few strokes.

Eldredge [50] presented the use of a viscous vortex particle method for the simulation of the flow produced by a two-dimensional rigid wing in pitching and plunging motion at a moderate Reynolds number. This method has the natural advantages that the correct velocity behavior at infinity is automatically accounted for and computational particles are only required in vortical regions of the flow. The application of this method to a pitching and plunging elliptical wing was presented for Reynolds number 550.

Kurtuluş et al. [3]-[51] performed a study to propose a simplified analytical model for prediction of the forces in order to find optimum parameters to generate maximum lift during flapping motion in hover, by using numerical methods, analytical models and experiments techniques. PIV technique was employed in experimental studies. A great number of cases were investigated involving the changes in the parameters such as angle of attack, location of start of change of incidence, location of start of change of velocity, axis of rotation, and Re number. In addition to the instantaneous aerodynamic forces, pressure distributions and vorticity contours, the average lift and drag coefficient values were also calculated. The experiments were performed as a part for the validation of numerical simulations. The model developed for the aerodynamic forces was an indicial method based on the use of the Duhamel Integral and the results obtained by this model were compared with the ones of the numerical simulations. The results revealed that the most influencing parameter is the starting angle of attack.

Sarıgöl et al. [4] analyzed the aerodynamics of two-dimensional and three dimensional flapping motion in hover in incompressible, laminar flow at low Reynolds number regime. To understand the physics and the underlying mechanisms of the flapping motion both numerical tools (Direct Numerical Simulation, DNS) and experimental tools (PIV) were used for two-dimensional and three-dimensional flow fields around symmetric and cambered airfoil profiles at Reynolds number 1000 for different angle of attack values. The obtained results were then analyzed in terms of aerodynamic force coefficients and vortex dynamics. The results showed that the lift coefficient is strongly dependent on the angle of attack regardless of the profile thickness and higher lift coefficient peak values are observed for thinner profiles and for increasing angles of attack. It was also observed that the vortex pattern is changing for different profile thickness values. The shedding of leading edge vortex and the detachment of vortices from the profile occurred earlier as the thickness increased.

A detailed numerical investigation of hovering mode in flapping motion was performed by Akay et al. [52] to find out the effect of some geometrical parameters, such as the airfoil profile shapes, thickness and camber distributions and as well as the flapping motion kinematics on the aerodynamic force coefficients and vortex formation mechanisms at low Reynolds number. The numerical analysis tool was a DNS code using the moving grid option. Laminar Navier-Stokes equations were used for prescribed kinematics in the Reynolds number range of 10^1-10^3. Computed aerodynamic force coefficients were compared for the profiles having different centers of rotation and angles of attack. Also, two different sinusoidal flapping motions were analyzed. Force coefficients and vorticity contours obtained from the numerical simulations were compared to experimental studies found in the literature. The results revealed that the validation of the present computational results with the experimental results available in the literature concludes that present numerical method can be a reliable alternative to experimental techniques.

In the study conducted by Başkan et al. [53] the aerodynamic performance of symmetrical and cambered airfoil profiles moving on different trajectories, namely linear and figure-of-eight flapping motions in hover, were covered to investigate and compare instantaneous aerodynamic force coefficients and vortex dynamics of these trajectories. Two-dimensional numerical simulations were carried out for laminar incompressible flow at low Reynolds number, namely Re=1000. Two-dimensional Navier- Stokes equations were solved on an O-type moving domain to obtain the pressure and velocity fields. The computed pressure and velocity fields were then used for the characterization of vortices in the flow field. The characterization of vortices in the flow field has a great importance in understanding the physics of the flapping motion and the generation of lift. The unsteady mechanisms that are responsible for the generation of aerodynamic forces were interpreted by the use of vortex mechanisms.

CHAPTER 3

NUMERICAL AND EXPERIMENTAL SETUP

3.1 Numerical Setup

Unsteady, laminar, incompressible, two dimensional flow fields around flapping airfoils have been analyzed numerically with commercially available CFD Package FLUENT 6.26.

3.1.1 Governing Equations

Two dimensional, time-dependent Navier-Stokes equations are solved using the finite-volume method for an incompressible flow [54]. The governing mass and momentum equations are described respectively by the following relations:

$$\frac{\partial \rho}{\partial t} + \nabla \cdot (\rho \vec{v}) = s_m \tag{3.1}$$

$$\frac{\partial}{\partial t}(\rho \vec{v}) + \nabla(\rho \vec{v}\vec{v}) = -\nabla p + \nabla \cdot \tau + p\vec{g} + \vec{F} \tag{3.2}$$

In Equation (3.2), τ stands for the stress tensor and is given as:

$$\tau = \mu\left[\left(\nabla \vec{v} + \nabla \vec{v}^{T}\right) - \frac{2}{3}\nabla \cdot \vec{v}I\right] \tag{3.3}$$

In this equation, μ stands for the molecular viscosity, I is the unit tensor and the second term on the right hand side is the effect of volume dilation.

In numerical solutions, the motion of the airfoil was modeled with FLUENT's dynamic mesh feature by flapping the body and the whole grid with predefined equations of motion. The flapping motion was introduced to the software with the help of User Defined Function (UDF) compiled in C.

The UDF transmits the information of velocity as the solution is being processed at each time step. In Fluent, the motion introduced with UDF can be applied individually to zones, i.e. wall, grid, velocity inlet etc. In case of numerical solution with moving airfoil with stationary grid, it is necessary to use the appropriate dynamic mesh methods, i.e. smoothing, layering or remeshing as the motion of the wall should be accompanied with the deformation or regeneration of the mesh along with the movement. In the current study, in order to get rid of negative cell volume problem in the boundary layer and cells of the computational grid, the motion interposed by the UDF was applied to the wall, grid points and the boundary conditions.

Governing equations solved by FLUENT to acquire unsteady solution for the flapping airfoil case change with the introduction of grid velocity. For a general scalar ϕ on an arbitrary control volume V, the integral form of the conservation equations can be written as follows:

$$\frac{d}{dt}\int_{V} \rho\phi dV + \int_{\partial V} \rho\phi\left(\vec{v} - \vec{v}_g\right)\cdot d\vec{A} = \int_{\partial V} \Gamma\nabla\phi \cdot d\vec{A} + \int_{V} S_{\phi} dV \qquad (3.4)$$

In Equation (3.4), $\vec{v}_g$ represents the grid velocity of the moving mesh, Γ is the diffusion coefficient and S_{ϕ} is the source term for ϕ.

3.1.2 Computational Grid

An O-type structured hyperbolic grid is generated using the commercial grid generation software "Gridgen". The grid domain used in the calculations consists of approximately 20000 (220×90) cells located within a domain of 15 chord lengths of radius. There are 220 grid points on the airfoil surface and the first normal grid point is located at a distance of 10^{-3} chord lengths from the airfoil surface.

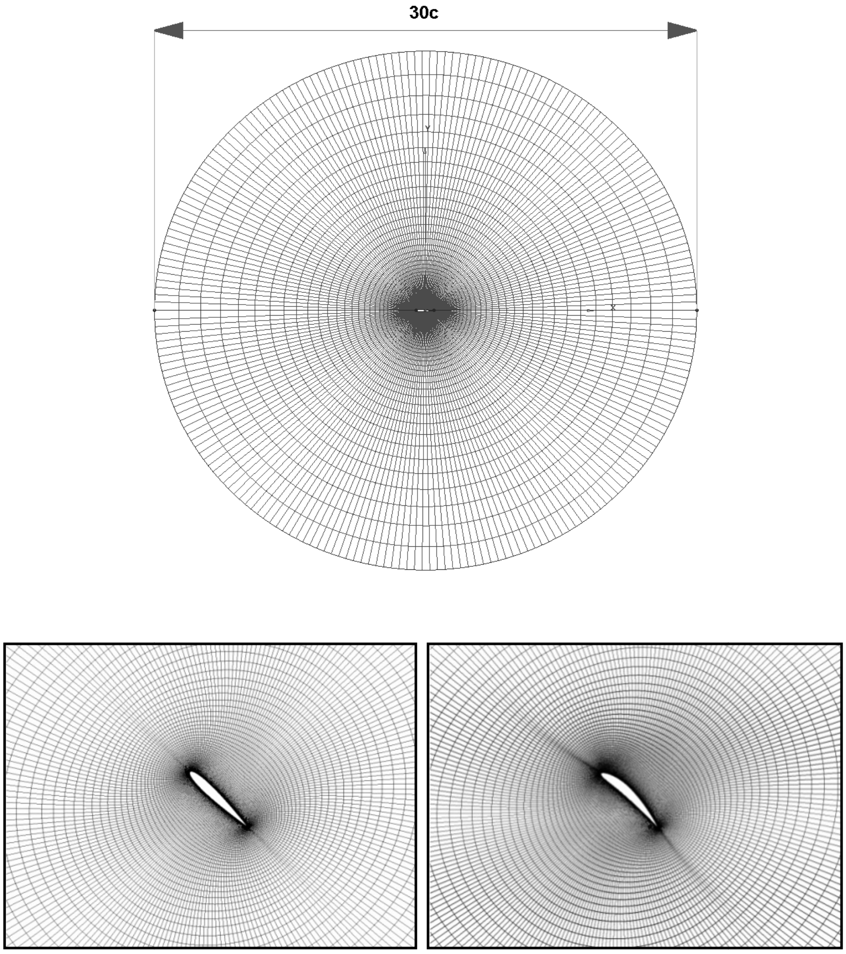

Figure 3.1 Computational grids around the airfoil surface

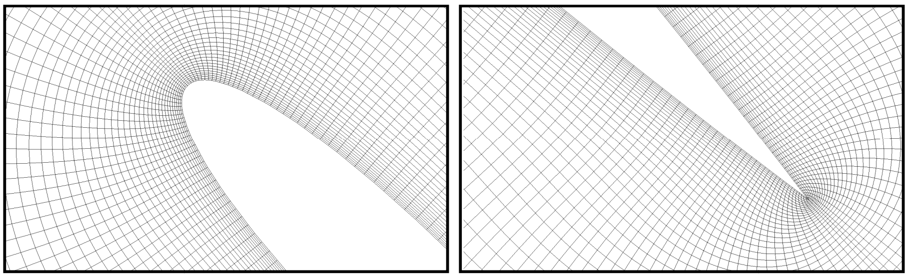

Figure 3.2 Computational grids around the airfoil surface (close view)

3.1.3 Selection of Grid size and time-step

In order to perform the unsteady flow simulations it is necessary to define the maximum grid size, minimum time-step and maximum total simulation time. In the present study, due to the harmonic nature of the flapping wings, periodicity is set as the criterion to achieve the convergence of the solutions. Hence, to reach the desired periodic flow patterns excessive simulation times are necessary. This excessive computational time limits the freedom in selecting the grid size and the time-step. Therefore, very small grid sizes and very small time steps must be chosen in order to achieve the stability of the computational scheme. With increasing number of grids and very small time steps very large simulation times are necessary to achieve the required periodicity of the flow. Since for the unsteady calculations the moving mesh solver of Fluent is used and due to the fact that this solver is of 1st order which necessitates even smaller time steps to be used, this causes the computational times to become even more excessive. Hence an optimization of the grid size and the time step used for unsteady flow calculations becomes inevitable.

To determine the optimum grid size and time step, different grid sizes and time steps are studied during this simulation. The grid sizes used were 20000 (220x90), 30000 (238x125) and 60000 (400x125) cells and the total number of time-steps used were 1000, 2000 and 5000 within one period of oscillations for NACA 0012 airfoil around which O-type grid is generated [55]. Linear flapping motion is used at a Reynolds number of Re=1000 and α=45° and the results of Kurtuluş [3] (Figure 3.3) are considered as a benchmark to decide on the appropriate grid size and the time step used during the calculations.

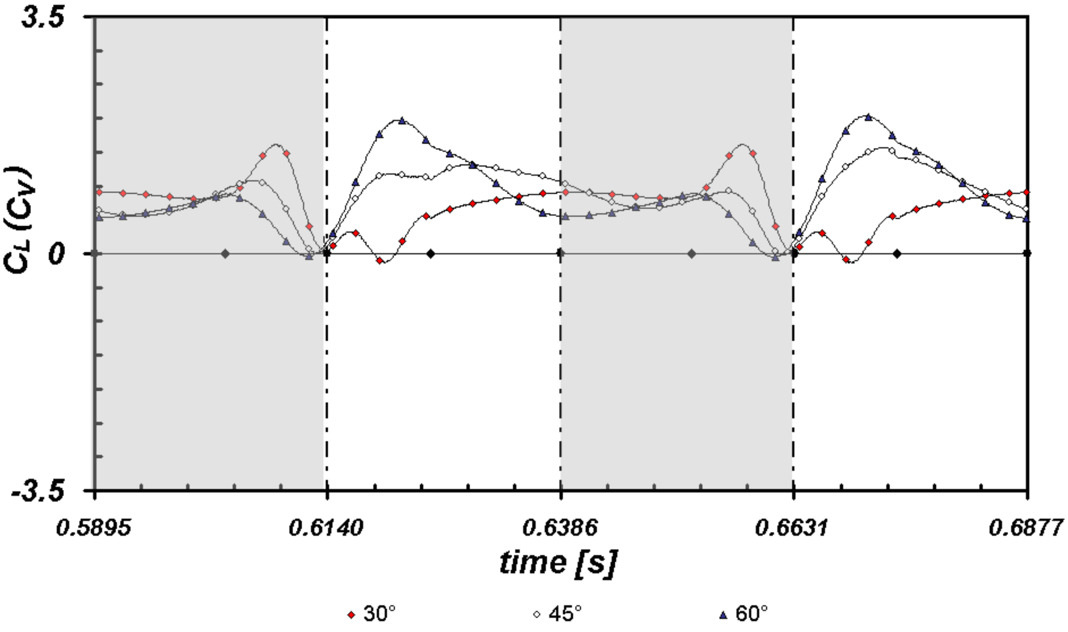

Figure 3.3 Lift coefficients (vertical force coefficients) of NACA 0012 for B=0 and Re=1000 at 7th period, Kurtuluş [3]

In order to investigate how strongly the solutions depend on the grid size the vertical force coefficients (C_V) calculated for Re=1000 and α=45° are plotted in Figure 3.4 for various grid sizes used. The results of grid sizes with 30000 and 60000 cells deviate from the results of Kurtuluş [3]. This is due to the fact that the number of the time-step used should be larger than 5000 for these cases, which means that the finer the grids are made, the smaller the time-step has to be chosen according to the time-step (stability) criterion.

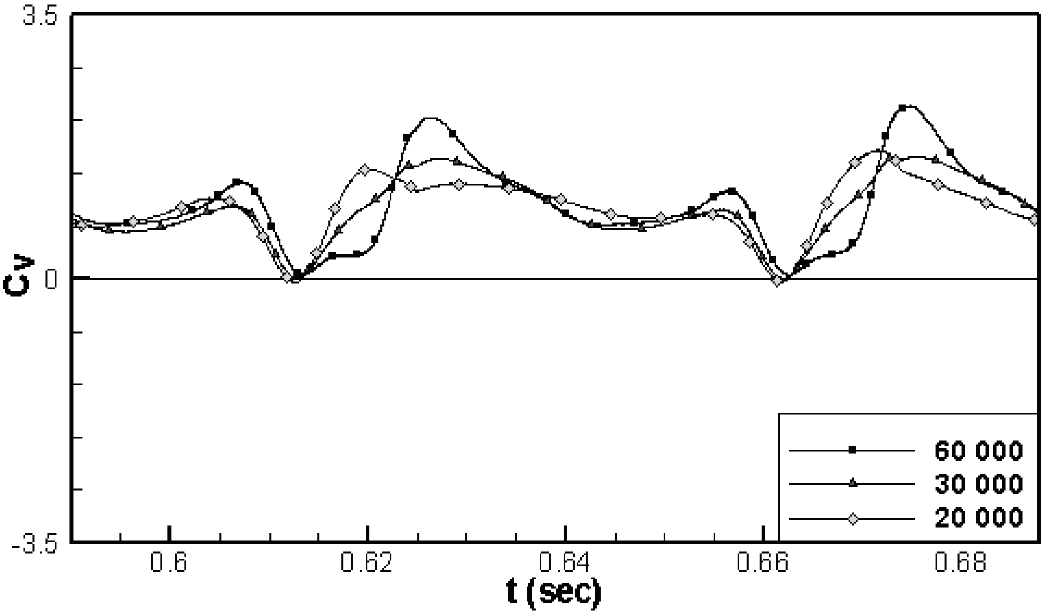

Figure 3.4 Effect of grid size on lift coefficients at a fixed time-step, T/5000

It is clearly visible from the results presented in Figure 3.5 for the variation of the lift coefficient during one period of flapping motion, the calculation done for 1000 time-steps deviates slightly from the other two solutions whereas the results for the case of 2000 time-steps coincides exactly with those of 5000 time-steps. It is clear that the simulation case with 5000 time-steps is relatively accurate when compared to results of Kurtuluş [3] (Figure 3.3). However, when the computational costs are taken into account, 2000 time step simulation becomes an efficient choice since the cost for 5000 time steps is 2.5 times more expensive.

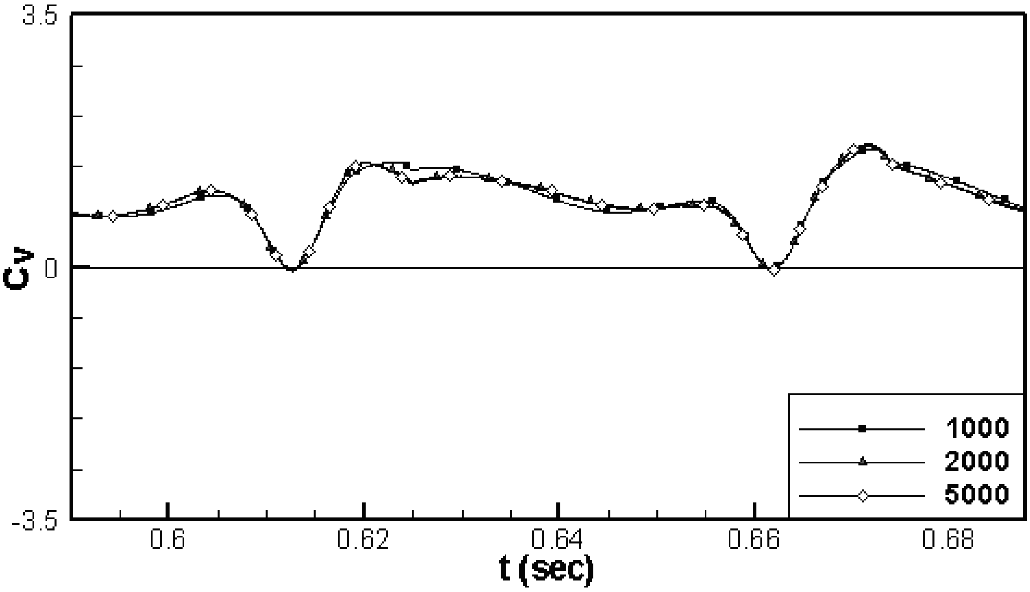

Figure 3.5 Effect of number of time-step on vertical force coefficients at a fixed grid size, 20000

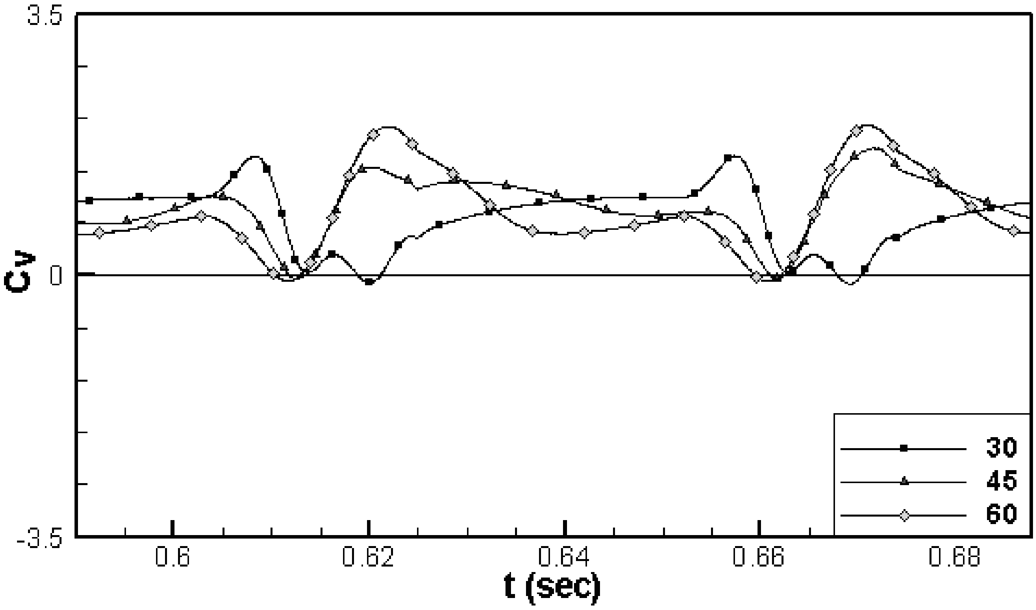

Figure 3.6 Vertical force coefficients of NACA 0012 for B=0 and Re=1000 at 7th period obtained after time step and grid size selection studies

The vertical coefficient variations at three different angle of attack values for Reynolds number of 1000 computed by using the mesh with 20000 cells and 2000 time-steps per period are presented in Figure 3.6. When the results acquired with the selected mesh and time-step are compared to the results of Kurtuluş [3], they show good agreement. Therefore, the mesh with 20000 cells and 2000 time-steps per period are chosen to be used throughout the study.

The influence of the outer boundary or the radius of the disc of the computational domain (influence of the far-field location) is also investigated for various values of chord lengths i.e. 10, 15 and 20 chord lengths. Considering the relative error of the computations and the computational cost it is found that a radius of 15c for the outer boundary of the computational domain becomes a reasonable and optimum choice for the present numerical calculations.

3.1.4 Computation Strategies

As stated previously, for numerical solutions, a commercial CFD Package FLUENT 6.26 has been employed using its incompressible flow solver option. First order upwind spatial discretizations and pressure-velocity coupling with PISO algorithm have been used as solution methods. Most of the numerical computations have been carried out at a Reynolds number of 1000 and the flow is assumed to be laminar at this Reynolds number. In previous studies, at Reynolds number of 20000, flow is assumed to be fully laminar and the numerical solutions were performed accordingly [56]. Moreover, the current study focuses on the interaction of large scale vortices (leading edge and trailing edge vortices) and therefore it is acceptable to neglect the effect of turbulence.

No-slip wall boundary conditions are implied on the airfoil surface. The far field is described as the pressure outlet. In hover condition, the far-field pressure is taken to be the standard air pressure.

Non-dimensional time step value was taken as 0.0005. The convergence criteria for momentum and continuity residuals have been set to be 1x 10^{-6} but the solution converged as the residuals reached a value of 1x 10^{-4}. For each time step, 60 iterations have been performed in order to satisfy the convergence criteria. Numerical solutions have been performed for 16000 non-dimensional time steps.

3.2 Experimental Setup

Experiments were conducted in a small scale water tank facility having the dimensions of $1\text{m} \times 1\text{m} \times 1.5\text{m}$ in the Aerospace Engineering Department of Middle East Technical University. The tank is made of altuglass (a type of proprietary acrylic) in order to apply nonintrusive experimental techniques, i.e. Particle Image Velocimetry (PIV), and filled with still pure water.

Experiments were performed using a symmetric airfoil profile; NACA 0012 and a cambered airfoil profile; NACA 6412. The chord length and the wing span of the airfoils are 6 cm and 50 cm, respectively. The center of rotation is located at the quarter chord length of the airfoil from the leading edge. The experimental wing models are made of plexiglass, which is transparent and allows the laser light to illuminate both the suction and the pressure sides (Figure 3.7). During the experiments, the airfoil was translated and rotated according to the motion kinematics scheme as used in the numerical simulations.

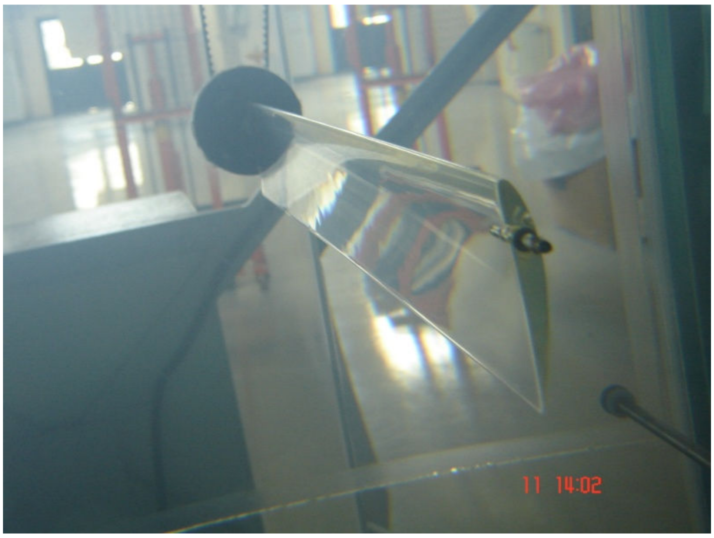

Figure 3.7 Experimental wing model

In order to ensure the two-dimensionality of the flow measurements the experimental model was placed between two endplates which are also made of plexiglass. Dimensions of the endplates are 90 cm in length and 50 cm in width. The airfoil and the endplates were mounted on a single assembly and translated together during the experiments.

Flapping motion of the airfoil was achieved by a step-motor mechanism which is placed outside the water tank. The system consists of two step motors. The first motor gives the translational motion to the assembly of wing and end plates through a power screw whereas the second one is used for the rotation of the wing. Thus, the system is capable of achieving linear flapping motion of the airfoil and cannot accomplish figure-of-eight motion. There is a ± 0.5 degree error in setting of the angles and the program is accurate to the second digit after decimal point. Maximum achievable translational speed is 4 cm/s. The power screw moves 4 mm at each revolution of the main step motor. Step motors which are controlled for velocity in an open-loop PC have 200 steps per revolution. The flapping motion for the experiments is implemented exactly the same way as was done in the numerical studies. In every 100 ms time interval, velocities and angles of attacks were calculated and sent to the upper mechanism.

Time dependent velocity fields around the flapping airfoil were acquired by using the Particle Image Velocimetry (PIV) method. DANTEC PIV System consists of a laser, two CCD cameras, a Flow Manager hub and a computer with a commercial data acquisition and post-processing software, namely Flow Manager. Detailed information about the PIV method and the DANTEC PIV system will be given in the following section.

The experimental setup which was used in the current study is same as that had been used by Sarıgöl [4]. The complete experimental setup is shown in Figure 3.8.

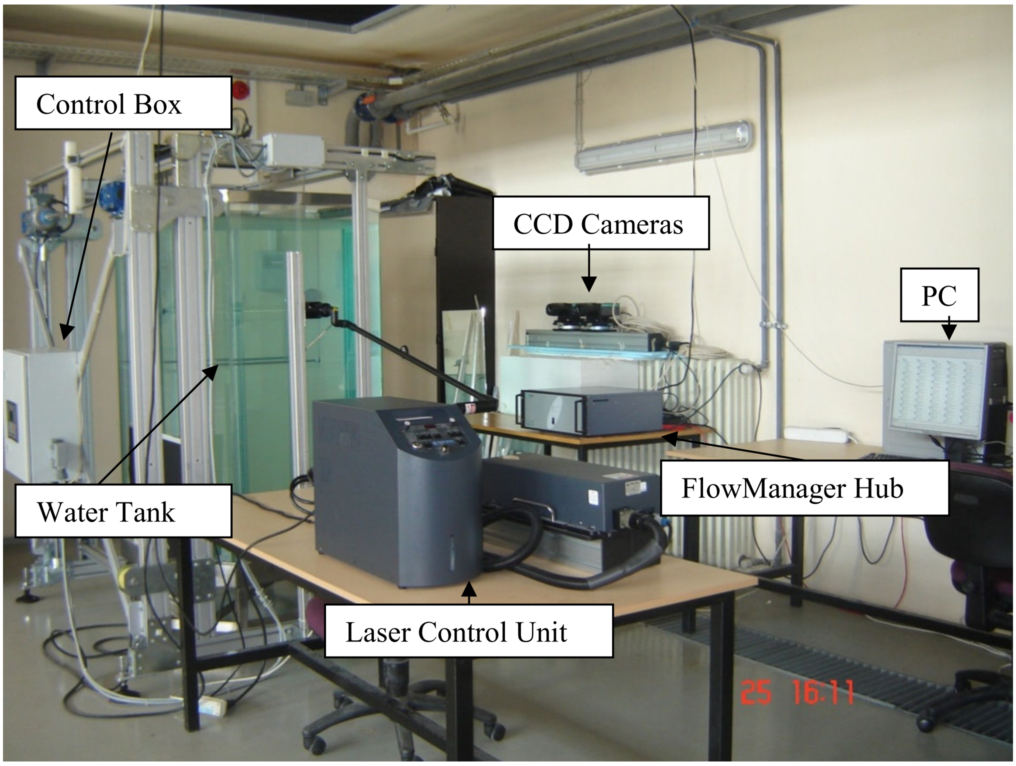

Figure 3.8 Experimental setup

In order to reduce the effect of the end plates, experiments were conducted at the mid-span of the wing. As noted before, hovering is a special case of flapping motion for which the free stream velocity is zero therefore it is plausible to perform PIV measurements in a water tank. Before starting the measurements the airfoil was set in motion for duration of at least 7 periods in order to achieve the periodicity of the flow. The Reynolds number based on the chord length and the maximum translational speed in x-direction is 1000.

3.2.1 Experimental Method – Particle Image Velocimetry

As indicated before, in the experimental part of the study, Particle Image Velocimetry (PIV), which is an advanced non-intrusive flow measurement technique, was employed in order to obtain the time dependent velocity fields and visualize the flow field around the flapping airfoil. In this section, brief information about the PIV technique is presented and the related post processing techniques are explained.

3.2.1.1 Basic principles of PIV

PIV is a non-intrusive flow field measurement technique. Basic principles of PIV method are given in Figure 3.9.

During the measurements via PIV, the quantity actually measured is the distance traveled by the particles in the flow within a known time interval. In order to perform that, particles are seeded into the flow. Seeding depends on the characteristic of the flow which is intended to be examined. Seeding particles should have suitable properties to follow the motion of the flow faithfully. Moreover, for the detection of particles' movement, a light sheet is used to illuminate the area of interest in the flow field. The illuminating laser sheet is pulsed to create stroboscopic effect, which means that the movement of seeding particles is paused with a certain time interval. This time interval is represented in the denominator of the equations indicated below.

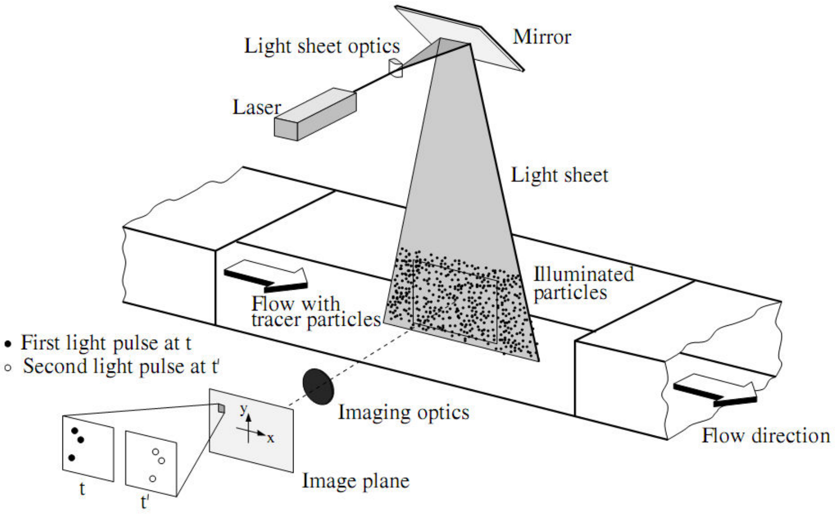

Figure 3.9 Basic principles of PIV, adapted from Raffel et al. [57]

$$u(x,t) = \frac{\Delta x}{\Delta t} \tag{3.5}$$

$$v(y,t) = \frac{\Delta y}{\Delta t} \tag{3.6}$$

In order to determine the position of seeding particles, a CCD-camera (CCD: Charged Couple Device) is placed at right angle to the light sheet. Moving particles appear as illuminated points on the dark background. The CCD-camera and laser are synchronized and thus the first image acquired at the first light pulse of the laser is saved on frame 1 of the camera, and the second pulse is saved on frame 2.

After acquiring the images, it is necessary to find out the velocity of the particles. To achieve this, each camera images are divided into rectangular sub domains which are called the interrogation areas or regions. Displacement vectors of each particle are obtained by using these interrogation areas. Interrogation fields, which are attained during the first and second pulse, are interrelated so that the average displacement of each particle can be calculated within a specific time interval which is the time between pulses. Afterwards, by using the basic formulae pointed out before (Equation 3.5 and Equation 3.6), the displacement vectors are turned into the average velocity vectors and thus a map of raw velocity vectors are acquired.

In order to perform the correlations faster, FFT-processing technique is used. It should be taken into account that, when using this method, there will always be an output data whether the input data are meaningful or not. Thus, it is necessary to corroborate the acquired vector maps. That explains why the vector maps which are obtained after the correlation are named raw vector maps. Consequently, the last step is to apply some kind of validation algorithms and perform further analysis. During the validations, incorrect velocity vectors can be detected and removed[58].

In summary, a basic PIV system consists of the seeding, illumination, cameras, synchronization, correlation, validation and further analysis. These are further explained below.

- **Seeding**

There exist a number of parameters that affect the motion of particles suspended in the fluid. These are particle shape, particle size, relative density of the particle to fluid, concentration of particles in fluid and the body forces.

Particle shape affects the drag force on the particle due to the surrounding fluid. Size and relative density of particles with respect to that of fluid's affect the response of the particle to any variation of the surrounding fluid velocity. Concentration of particles in the fluid influences the motion of each individual particle due to the interaction between particles themselves. Generally, this is neglected since the concentration of particles used is low. Body forces, especially gravity force in low speed flows, are effective in the measurements.

- **Illumination**

Generally, three different illumination methods are employed in PIV measurements. First one is the utilization of double cavity Q switched Nd: Yag laser that generates two pulsing beams which are merged and formed into pulsing light sheet by using optics. Second one is to use argon-ion laser that generates a continuous laser beam which is cut by shutter and final pulsing beam is developed into a laser sheet using optics. Third one is to use argon-ion laser that generates continuous wave beam which is scanned by rotating polygon mirror to create a pseudo light sheet.

- **Camera**

In PIV measurements, cameras are used to detect initial and final positions of particles in the flow. Difference between the two positions gives the displacement vector of that particle. Historically, PIV measurements were performed with the use of photographic films. In recent times, CCD cameras have been extensively used in PIV measurements. These cameras are capable of capturing instantaneous image map of the particles.

- **Correlation**

In recent PIV systems, two sequential maps are subsampled. The resolution of this sampling is called an interrogation area and these interrogation areas develop a regular array. With the help of these interrogation areas, the spatial shifting of the seeding particles can be observed from one sample to its counterpart in the second camera image. Then cross-correlation technique, the flowchart of which is shown in Figure 3.10, is generally used in order to obtain resultant velocity map.

Apart from the standard cross-correlation technique, in order to acquire more successful vectors in a larger area while capturing the flow details or to increase the dynamic range and the accuracy of the system, advanced correlation methods, such as adaptive correlation technique, can be used.

The basic principle of the adaptive correlation is its iterative procedure. The procedure starts with an initial guessed offset value (offset value is introduced from frame 1 to frame 2) and selected interrogation area size. Then acquired vector is validated and this vector is used to make estimation for the new correlation area offset. The new correlation process is carried out with a smaller interrogation area this time.

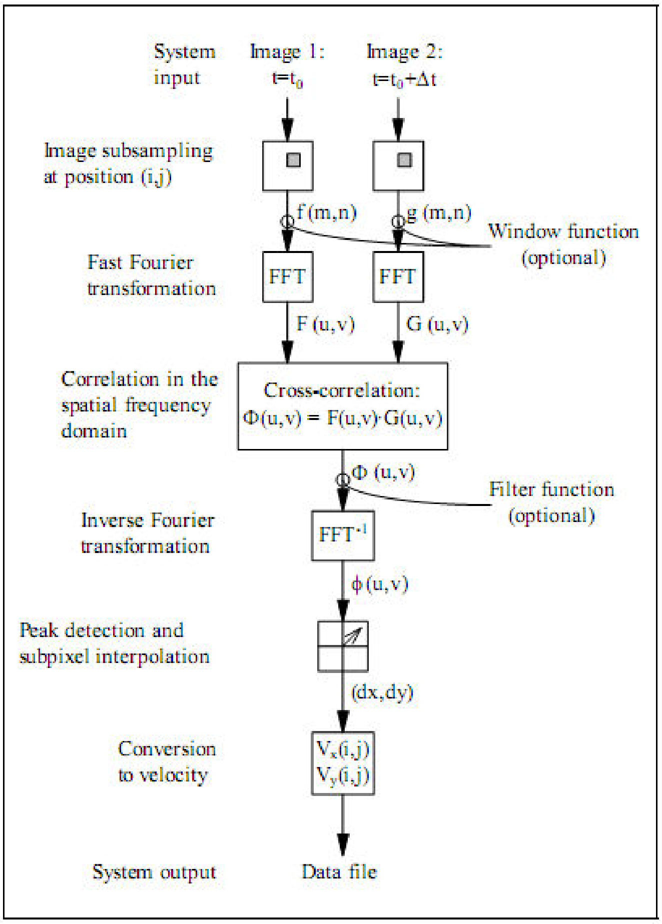

Figure 3.10 Processing flowchart of PIV – Cross correlation method [58]

Adaptive correlation method is beneficial in sense of capturing the particle images which have left the interrogation area during the time between pulses (the loss of these particle images is named as “in-plane dropout”) and thus increasing the signal strength. As a result of this augmentation, more successful vectors can be acquired when compared to the standard cross correlation technique.

As a result, adaptive correlation is helpful in two ways. First, PIV signal strength is increased by capturing the dropouts and secondly it is possible to refine the interrogation area by using adaptive window offset [58].

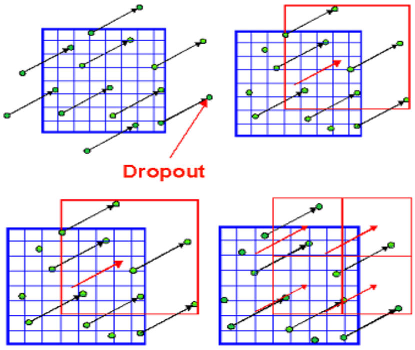

Figure 3.11 Capture of in-plane dropouts by using adaptive window offset [58]

- **Validation and further analysis**

It was earlier indicated that there will always be an output vector whether the input data is meaningful or not. Therefore, the aim of the validation methods is to recognize, reject and remove incorrect vectors and replace them with more correct ones. Latest PIV systems generally include validation methods based on logical mathematical algorithms. These validation methods include peak height ratios, velocity range validation, moving average, manual validation of vector maps, and masking to remove vectors from areas that are supposed to be free of any vector information. Moreover, filters can be employed to reduce the noise in the post-processing.

- **Image acquisition**

As stated earlier, quantitative flow images were captured with commercial DANTEC PIV system which consists of a laser, two CCD cameras, a FlowManager hub and a data acquisition computer with commercial acquisition and post-processing software, i.e. Flow Manager. In this section, steps followed during the PIV measurements are briefly explained. The schematic of the PIV setup is shown in Figure 3.12.

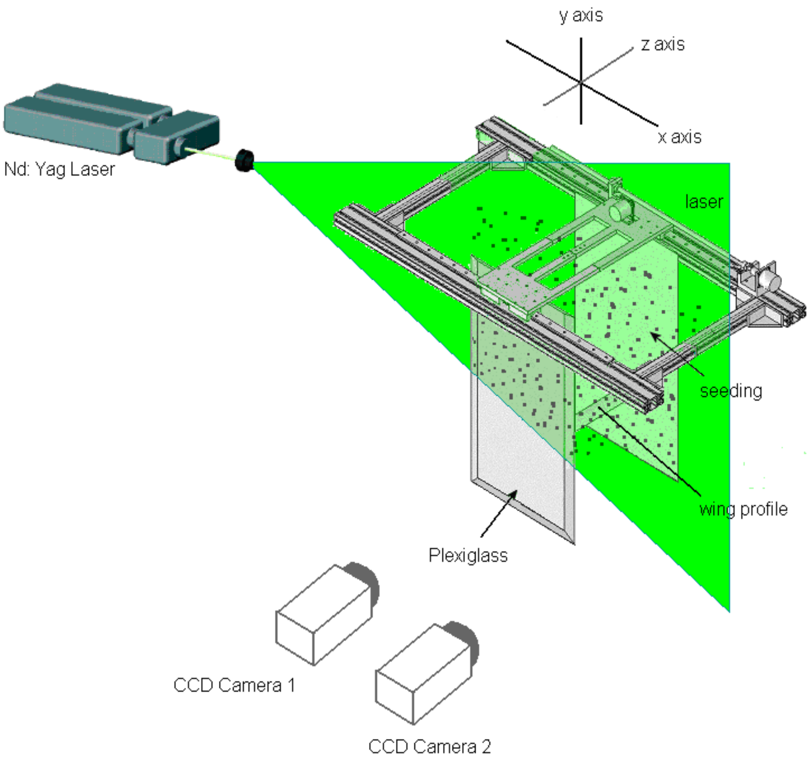

Figure 3.12 The schematic of PIV setup

Pure water (1.5 m^3 in volume) inside the tank was seeded with 2.5 grams of silver coated hollow glass spheres with a mean diameter of 10μm. Some specifications of the seeding material are given in Table 3-1.

Table 3-1 Properties of seeding material

Mean particle size (μm)	10
Size distribution	2-20 μm
Particle shape	Spherical
Density (g/cm3)	1.4
Melting point (° C)	740
Material	Borosilicate glass

The flow was illuminated by a New Wave Solo-PIV 120 Nd: Yag laser with two cavities each providing 15 Hz repetition rate. The maximum output energy is 120 mJ per pulse at 532 nm wavelength with pulse duration of 3-5 ns.

Quantitative flow images were captured with two 10 bit Hi-Sense cameras with 1280×1024 pixel resolution and 8 Hz frame rate. For each experimental case, 102 images were recorded at 2 Hz frame rate covering the whole period of the flapping motion. Two identical cameras are positioned side by side to capture a wider field of view around the flapping airfoil. The magnification factors for the cameras were 1:28.395 and the resulting physical measurement plane for each camera was $246.2\text{mm} \times 187.5\text{mm}$.

The data acquisition was performed by using the data acquisition software of the PIV system and the control software of the step-motor system together. It is possible to start the data acquisition in the Flow Manager software at an arbitrary time manually or at a specified time with an external trigger. During the experiments, in order to start the acquisition at the beginning of the period of flapping motion, external trigger mode was used and the external trigger signal was generated via control software of the motor system (Figure 3.13) which is capable of obtaining the position, the velocity and the angle of attack of the airfoil in real time.

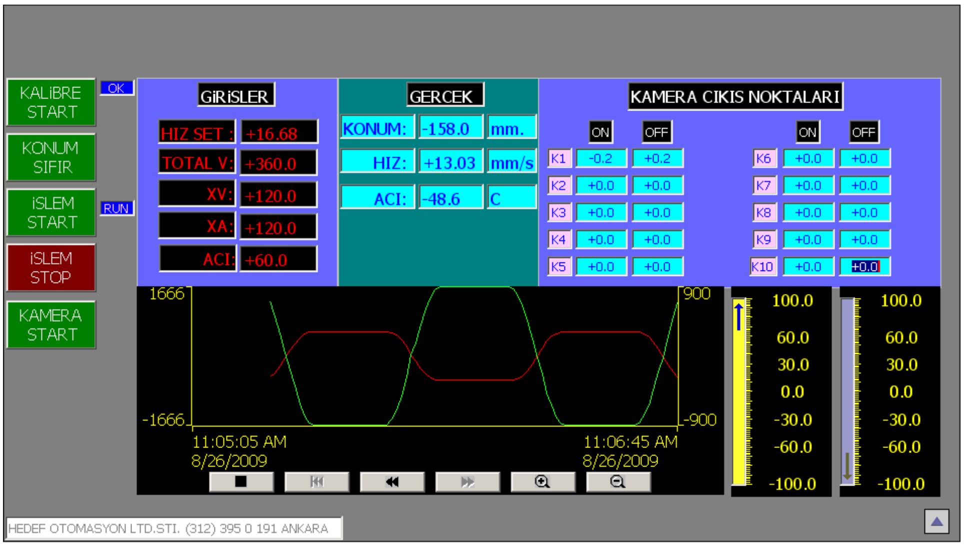

GiRiSLER

HIZ SET : +16.68
TOTAL V: +360.0
XV: +120.0
XA: +120.0
ACI: +60.0

GERCEK

KONUM: -158.0 mm.
HIZ: +13.03 mm/s
ACI: -48.6 C

KAMERA CIKIS NOKTALARI

	ON	OFF		ON	OFF
K1	-0.2	+0.2	K6	+0.0	+0.0
K2	+0.0	+0.0	K7	+0.0	+0.0
K3	+0.0	+0.0	K8	+0.0	+0.0
K4	+0.0	+0.0	K9	+0.0	+0.0
K5	+0.0	+0.0	K10	+0.0	+0.0

Figure 3.13 Interface of the step-motor control software

Before performing the PIV measurements, the step-motor system was calibrated for accuracy of the position and angle of attack. The airfoil was held in the middle of the water tank. The linear speed, initial angle of attack and positions for constant translational speed and angle of attack was introduced manually to the user-interface software of the step-motor system. After 7 periods of the motion of the airfoil, the software generated a 5 volt trigger signal. The signal was transmitted to the Flow Manager Hub and triggered the laser source and stereo cameras of the DANTEC PIV system and started the acquisition. The exact trigger time was introduced to the software through the snapshot check points in terms of position of the airfoil. It is possible to enter at most 10 different snapshot check points to the software and when the "camera-start" button of the interface software is activated the software also displays the instantaneous position, velocity and the angle of attack of the model.

- **Data analysis**

PIV images were recorded at 2 Hz in a double frame – single exposure mode. Time between pulses (time interval between two frames) was 80000 μs. This time interval was selected such that, in this time interval the seeding particle could not travel a distance greater than the quarter length of the interrogation window. A High-pass filter (Laplacian 5

$\times 5$) was applied to recorded images in order to obtain the details and remove the large scale gradients. The filtering process and its result are shown in Figure 3.14.

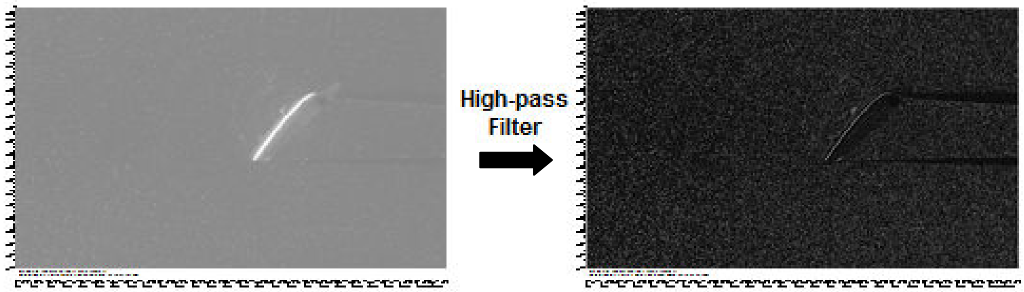

Figure 3.14 Application of High-pass filter to the recorded PIV image

The area on the image, which is covered by the shadow of the airfoil, does not contain vector information and should be eliminated. This elimination was performed by masking those areas on the images considered in the current study. Masks were generated on the top of the image maps and applied to both filtered images and vector maps which were acquired after the adaptive correlation procedure.

Filtered and masked PIV images were interrogated using adaptive correlation (Figure 3.15). The final interrogation area size was set to be 64×64 pixels with 50% overlapping in each direction. Number of refinement steps was determined to be 3, which means that the size of the interrogation area for the initial correlation process was 512×512 pixels. As a result, the physical area of measurement plane was represented 41×31 (1271) vectors. The grid resolution of the velocity vectors was 5.86mm $\times$ 5.86mm.

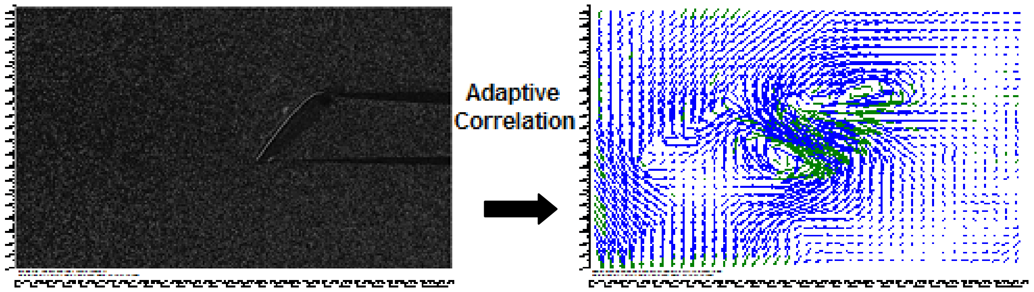

Figure 3.15 Application of adaptive correlation to the masked and filtered PIV image

As a next step, incorrect vectors, which were usually greater in length relative to meaningful vectors, were removed by using range validation. Vectors, which were outside a certain range, were rejected by estimating the expected range of velocities in the flow. These rejected vectors were replaced by the vectors estimated from the surrounding values by using moving-average validation. In the moving-average validation the average of the vectors in a rectangular neighborhood of a vector is calculated and compared with the vector. Moving average validation was performed for an averaging area of 3x3 pixels and with an acceptance factor of 0.1. Number of iterations was set as 3 for moving average validation.

In order to remove small scale noise from the validated vector map, average filter was employed. In theory, this filter substitutes each vector with the uniformly weighted average of the vectors in a neighbourhood of a specified size. Average filter was performed for a 3x3 neighbourhood of vectors.

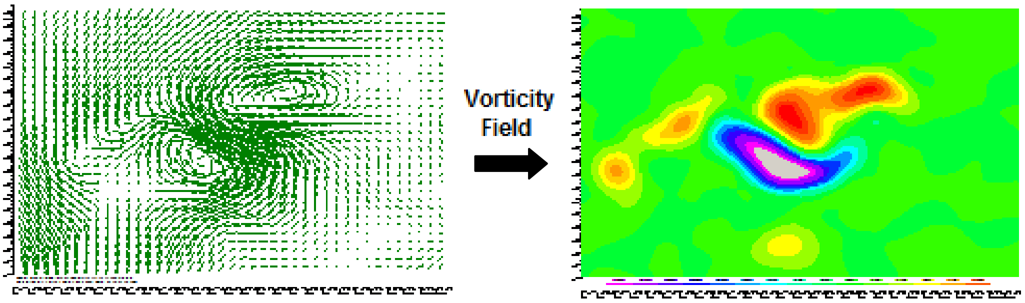

Figure 3.16 Derivation of vorticity field from the validated and filtered vector map

As the last step, vorticity fields were calculated based on 2-D vector maps (Figure 3.16). The vorticity fields corresponding to each vector map were derived via the Flow Manager Software; then, the data file was exported and scalar maps were plotted using the Tecplot Software.

CHAPTER 4

NUMERICAL RESULTS

The numerical studies were conducted in order to analyze the effects of the vertical motion of the airfoil on aerodynamic forces and find out the advantages of the figure-of-eight flapping motion over the linear flapping motion. A number of cases are investigated for different parameters which are the vertical amplitude of the figure-of-eight flapping motion (*B*), initial angle of attack (α), Reynolds number (*Re*), and the shape of the airfoil. The parameters, which were considered in the numerical solutions, are shown in Table 4.1. Instantaneous aerodynamic forces and vorticity contours were derived and compared throughout the study. Furthermore, the average vertical and horizontal force coefficient values and ratios of average vertical force to average horizontal force values were also acquired.

Table 4-1 Parameters investigated in numerical studies

B	0, 0.5c, 1c, 1.5c, 2c
α	30°, 45°, 60°
Re	200, 1000, 5000
A/F	NACA 0012, NACA 6412

The fluid was selected to be air for the numerical solutions. The values for the viscosity and density of air that were used in the calculations are $1.789\times10^{-5}\,kg/(m\cdot s)$ and $1.225\,kg/m^3$, respectively. As stated earlier, to ensure the periodicity of the flow around the airfoil, the entire calculation of domain is obtained during the 7th period of the flapping motion [3].

During the figure-of-eight motion, the airfoil moves in horizontal (x) and vertical (y) directions. In addition to its translation, the angle of attack of the airfoil also changes as explained in the detailed definition of the motion. The kinematics of the figure-of-eight motion is introduced in Figure 4.2 in terms of velocity in x-direction, velocity in y-direction, absolute velocity and angular velocity for a non-dimensional period of the motion.

In the following context of this thesis C_H denotes the coefficient of horizontal force component and C_V denotes the coefficient of vertical force component. Both of these coefficients are positive as indicated in Figure 4.1.

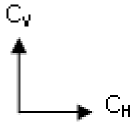

Figure 4.1 Global reference frame for force coefficients

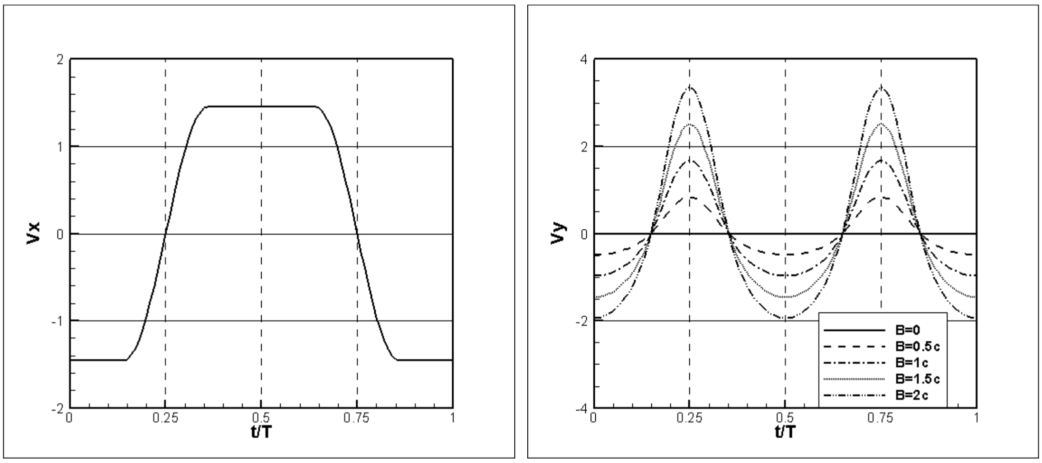

a- Velocity in x-direction (m/s)

b- Velocity in y-direction (m/s)

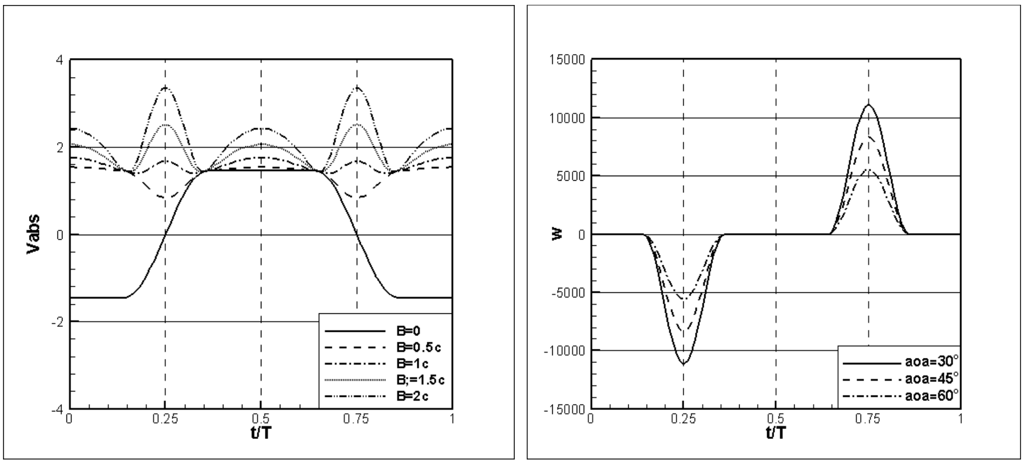

c- Absolute velocity (m/s)

d- Angular velocity (deg/s)

Figure 4.2 Kinematics of the flapping motion for Re=1000

4.1 Effects of Vertical Amplitude (*B*) of the Motion

In order to investigate the effects of vertical amplitude of the figure-of-eight motion, numerical solutions were carried out for five different vertical amplitude values, as evident in Table 4.1. For the case when B is equal to zero (B=0), the kinematics of the motion is the same as the linear flapping motion, as stated previously. Although calculations were performed for three different initial angles of attacks and for two different airfoils for each vertical amplitude value, only the cases for NACA 0012 with the initial angle of attack of 45^0 are presented in the current study for brevity.

For the cases considered for this section, instantaneous horizontal and vertical coefficient values are plotted and compared over one non-dimensionalized period for the vertical amplitude values covered in the study (Figure 4.3 and Figure 4.4). The non-dimensional time values for the highest and lowest vertical force coefficients are labeled with line A and line B, whereas, the non-dimensional time values for the highest and lowest horizontal coefficients are labeled with line C and line D, respectively. Moreover, instantaneous vorticity contours for lines A-B and C-D, which lay on horizontal and vertical force coefficient plots, are given in Figure 4.5 to comprehend the corresponding vortical structures which lead to maximum and minimum aerodynamic force coefficient values.

There exists two positive and two negative peaks in vertical force coefficient curves as the motion of the airfoil is axis-symmetric for one period of simulation. Positive peaks occur at the translational phase whereas; negative peaks happen during rotational phase of the motion.

Minimum values of the vertical force coefficient are acquired during the phase, in which the airfoil is moving in the upward direction with a relatively small horizontal velocity. During this phase, as the airfoil translates in the vertical direction with an angle of attack, a drag force is exerted on the airfoil at that instant with respect to motion reference frame, which is negative vertical force (negative lift force) in the global reference frame.

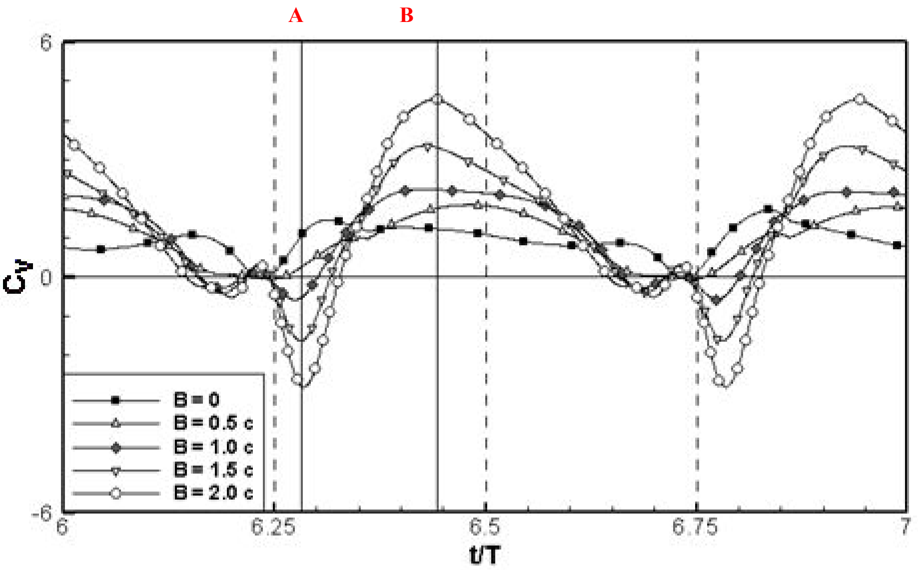

Figure 4.3 Vertical force coefficients of NACA 0012 for α=45°and Re=1000 at 7th period

On the other hand, maximum values of the vertical force coefficient are acquired at the non-dimensional time (line B), at which the airfoil moves with a negative y velocity, constant x velocity and constant angle of attack. The corresponding vorticity contours are shown in Figure 4.5 on the row labeled as B. It is evident that counter-rotating leading and trailing edge vortices are present on the upper surface of the airfoil for the figure-of-eight motion (B=0 is the linear flapping motion). The presence of these massive vortices creates a suction region and results in greater positive lifting coefficient. Furthermore, it is also evident that the maximum vertical force coefficient increases dramatically after the vertical amplitude value of 1.0 c. The reason for this increase can be shown as the lack of interaction of recently formed trailing edge vortex with the counter-rotating trailing edge vortex which is formed and shed during the previous stroke (Figure 4.5 and Figure 4.6). This condition results in the conservation of the strength of vorticity, increased suction and increased lifting coefficient.

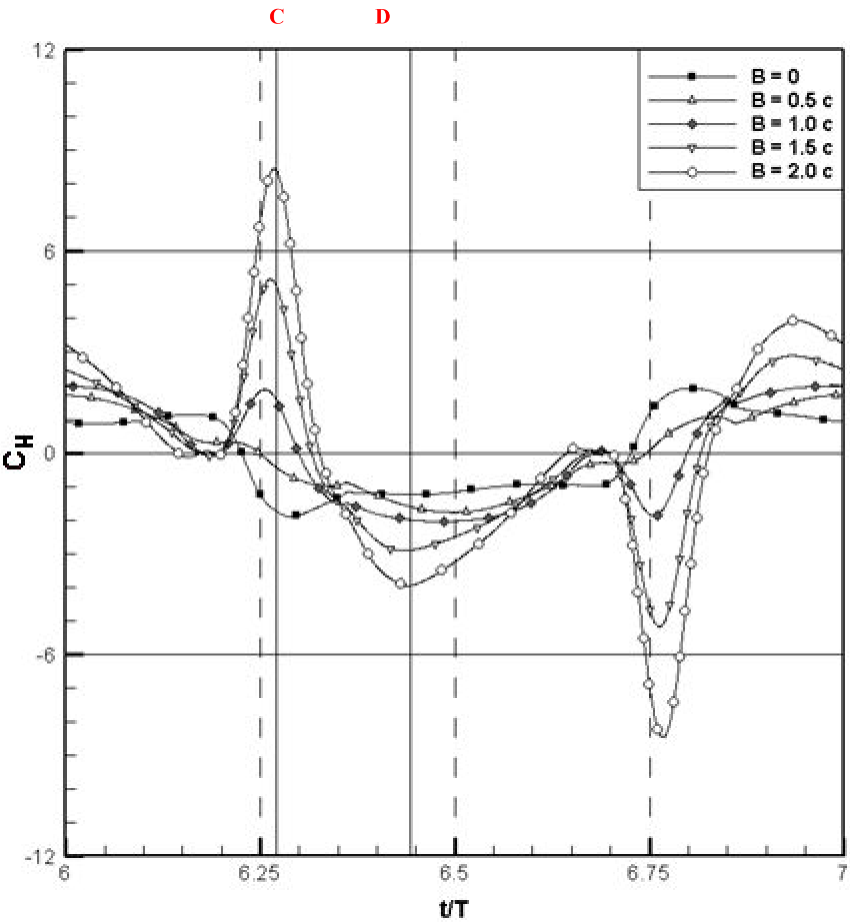

Figure 4.4 Horizontal force coefficients of NACA 0012 for α=45°and Re=1000 at 7th period

It is apparent that same type of mechanism plays a role in obtaining maximum and minimum horizontal force coefficients. In flapping motion, the force coefficient in the horizontal direction can either be the instantaneous drag or the thrust force based on the directions of velocity and force. If the components of velocity and force on the x axis is in the same direction or have the same sign, this means that a thrust force is exerted on the airfoil.

For maximums (line C), it is evident that during the vertical motion of the airfoil with an angle of attack, a lifting force is exerted on the airfoil with respect to motion reference frame (Figure 4.5). This condition adds up the horizontal force coefficient in positive direction in the global reference frame. Thrusting force is exerted on the body for that instant as the horizontal velocity and the horizontal force coefficient values have the same sign. For minimums it is evident in Figure 4.5 on the row D, leading and trailing edge vortices creates a suction region in the opposite direction of the motion and hence this region generates a dragging force in the motion reference frame. As the airfoil moves in the positive x-direction for the 2nd region of the figure-of-eight motion, dragging force counts for negative horizontal force in the global reference frame. Horizontal force production mechanism occurs in the reverse direction which results in the mirrored coefficient values for the 4th region of the motion.

When the cases for different vertical amplitude values are compared in terms of maximum and minimum vertical/horizontal coefficients, it is clear that greatest and smallest values are obtained for the case of $B=2.0\ c$. The minimum vertical and the maximum horizontal force coefficients for this case can be attributed to the relatively higher vertical velocity of the airfoil. On the other hand, the reason for the maximum vertical force coefficient and the minimum horizontal force coefficient can be shown as the massive leading and trailing edge vortices. Moreover, increased amplitude of the motion prevents the interaction between recently formed and previously formed vortices.

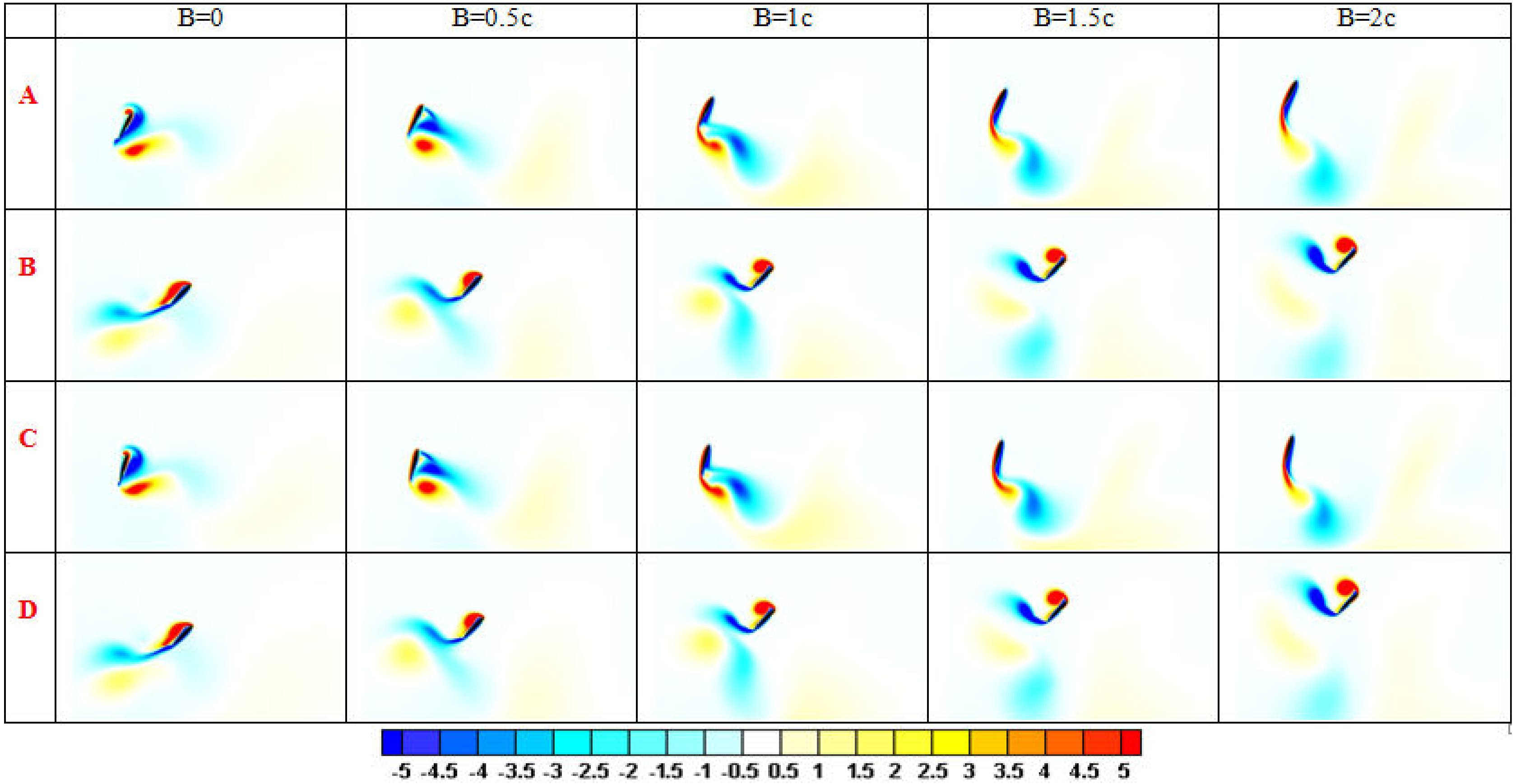

Figure 4.5 Non-dimensional vorticity contours corresponding to A-B and C-D lines

In Figure 4.6 and Figure 4.7, linear flapping and figure-of-eight motions (for *B=1.0 c* and *2.0 c*) are compared for two different airfoils in the sense of vortical structures over a period of the motion. The basic shedding mechanism for the figure-of-eight motion can be explained as follows; in the 1st region of the motion ($6<t/T<6.5$), counter-rotating leading and trailing edge vortices are generated and translate with the airfoil. During this translation, counter-clockwise rotating trailing edge vortex elongates and interacts with the clockwise rotating massive leading edge vortex. This interaction results in the decrease of strength of trailing edge vortex. At the end of 1st region, counter-rotating leading and trailing edge vortices are coupled and they convect upwards with their induced velocities. As the airfoil continues its motion in a vertical direction, recently formed clockwise rotating leading edge vortex elongates over the airfoil surface and then it increases the strength of trailing edge vortex that is formed in the 2nd region of the motion. Same vortex formation and interaction mechanism is apparent in the 3rd and 4th regions of the motion.

As stated before, with the increase of vertical amplitude, the interaction between the vortices which are formed in the 1st and 2nd region of the motions deteriorates. This absence of interaction results in stronger leading and trailing edge vortices which are beneficial in terms of lift enhancement. Actually, this outcome is the main advantage of the figure-of-eight motion.

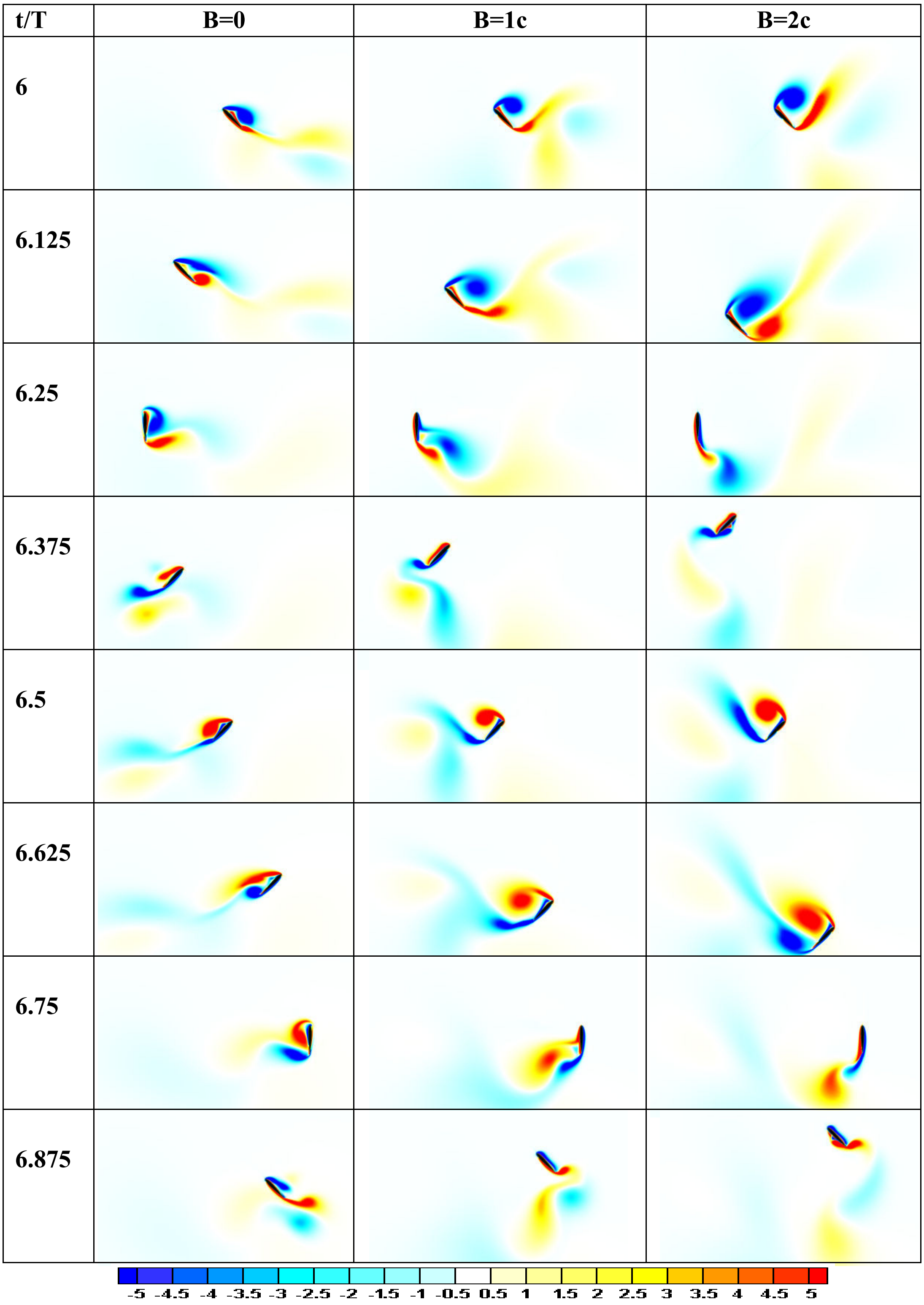

Figure 4.6 Non-dimensional vorticity contours of NACA 0012 during the 7th period for α=45° and Re=1000

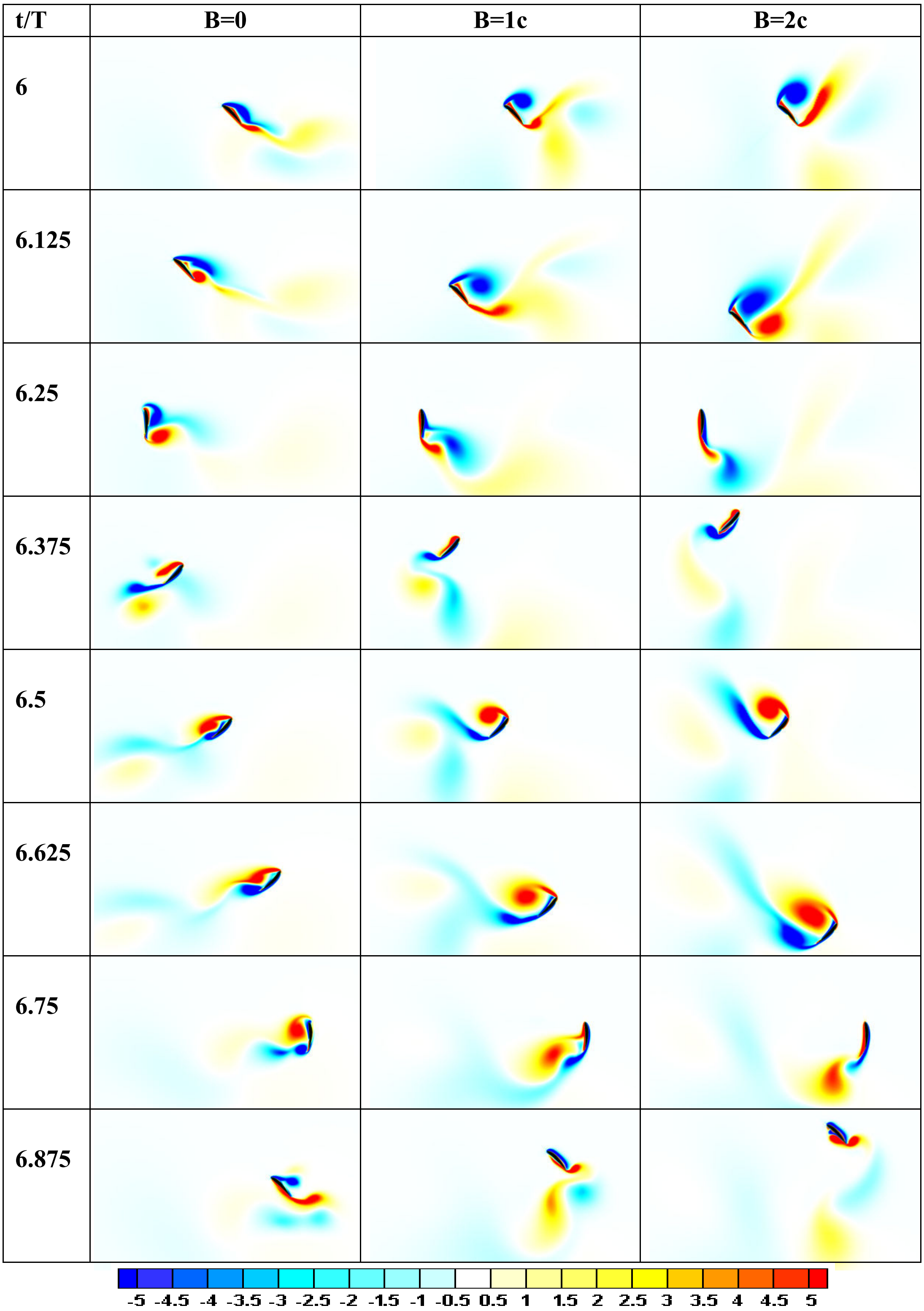

Figure 4.7 Non-dimensional vorticity contours of NACA 6412 during the 7th period for α=45° and Re=1000

4.2 Effects of Initial Angle of Attack

In this section, effects of initial angle of attack are investigated for three different angles for both linear flapping and figure-of-eight motion case.

In Figure 4.8 and Figure 4.9, vertical and horizontal force coefficients for NACA 0012 airfoil undergoing a linear flapping motion are plotted for the initial angle of attack values considered in the study.

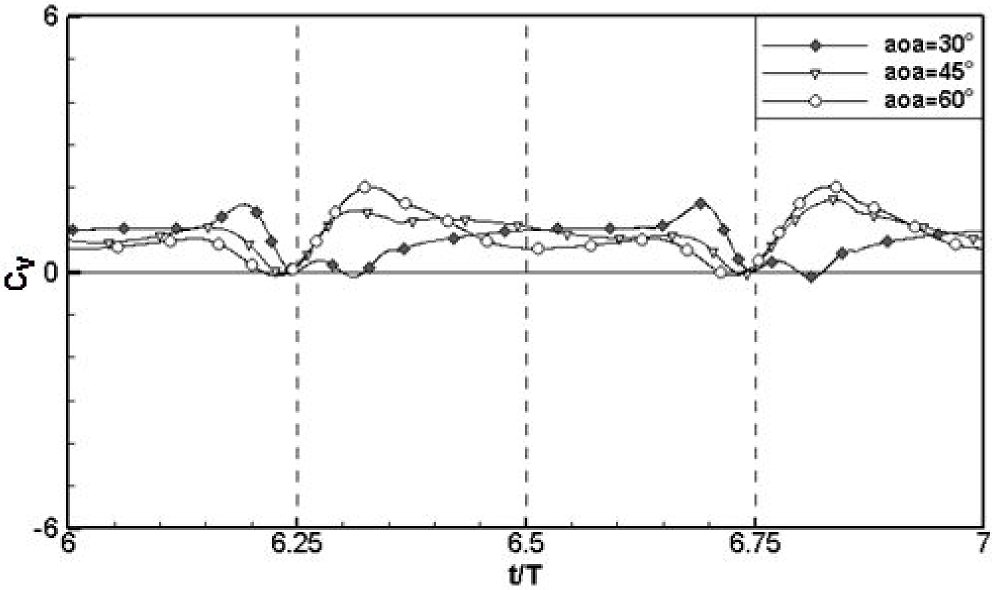

Figure 4.8 Vertical force coefficients of NACA 0012 for B=0 and Re=1000 at 7th period

It is evident in the vertical force coefficient plot that positive lifting force is generated at each instant of the motion due to the presence of leading edge vortex on the upper surface of the airfoil. As anticipated, higher angle of attack results in generation of massive vortices. These massive vortices increase the suction in the upward direction and hence the forces exerted on the body. The highest vertical and horizontal force coefficients acquired for the case of maximum initial angle of attack verifies the statement.

On the other hand, lower initial angle of attack means higher rotational velocities during the rotational phase. Higher pitching velocity results in a sudden increase in the vertical and horizontal force coefficient value as evident in Figure 4.8 and Figure 4.9 for the case of 30^0. Following to this, as the airfoil reaches the angle of attack of 90^0, the vertical force coefficient becomes zero. Then in the phase in which the airfoil starts its motion in the opposite direction, the vertical force coefficient has smaller values due to the decreasing angle of attack and interaction with recently formed vortices. This interaction leads to loss of vorticity and decrease of lift coefficient.

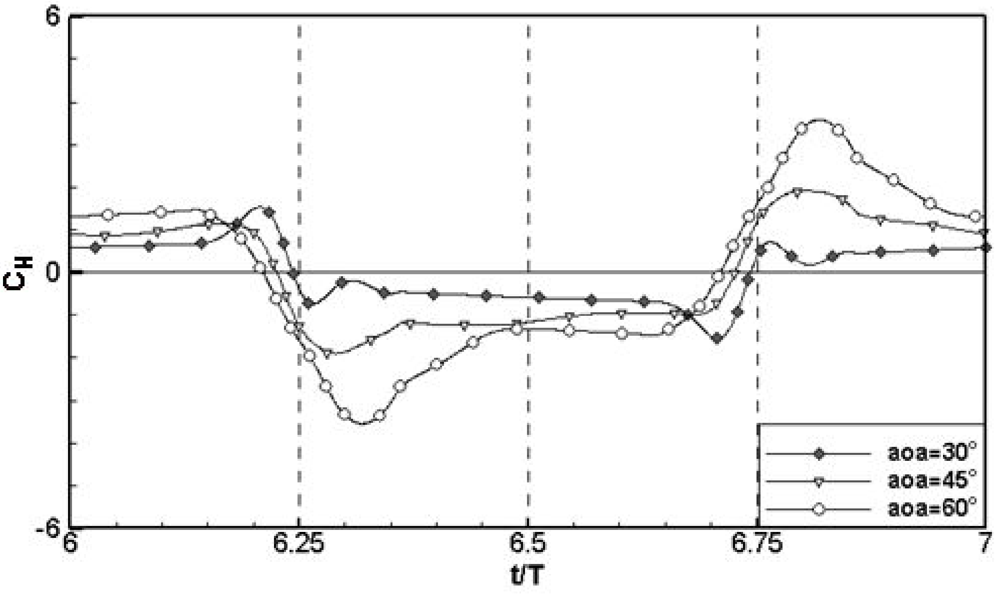

Figure 4.9 Horizontal force coefficients of NACA 0012 for B=0 and Re=1000 at 7th period

For linear flapping motion, there is no thrusting force production except very small time periods just before the end of 1st and 3rd region as evident in Figure 4.9. For the 2nd and 3rd region, negative horizontal force coefficient means drag force as the airfoil moves in the positive x-direction.

In Figure 4.10 and Figure 4.11, vertical and horizontal force coefficients are plotted for the figure-of-eight motion with the vertical amplitude of *B=2.0 c*.

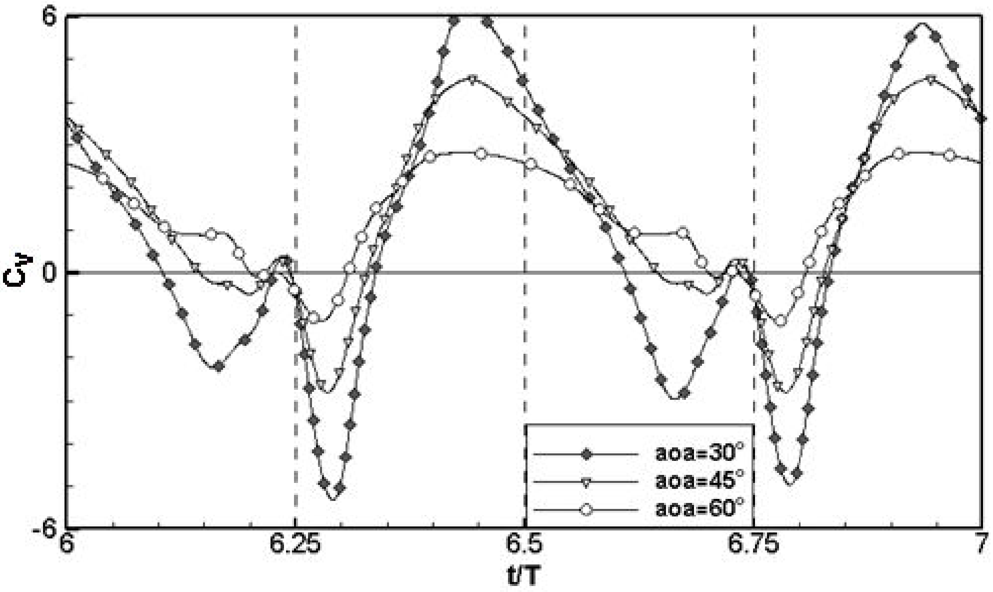

Figure 4.10 Vertical force coefficients of NACA 0012 for B=2c and Re=1000 at 7th period

It is possible to say that higher rotational velocity plays an important role in acquiring greater instantaneous vertical force coefficients during the rotational phase. As evident in Figure 4.10, for the case of 30^0 the smallest vertical force coefficient is acquired due to the increased rotational velocity. Increased rotational velocity results in generation of suction region near the trailing edge which increases the strength of trailing edge vortex. Moreover, this suction region results in the presence of effect of previously formed leading edge vortex while for other cases previously formed leading edge vortex is elongated and convected downwards direction. All these effects lead to a declined average lifting coefficient. On the other hand, during the translational phase of the motion, as the airfoil surface that counters the flow increases for a smaller angle of attack, the acquired lifting coefficient increases. The vertical flow coefficient values for the period 6.25<t/T<6.5 validates this statement.

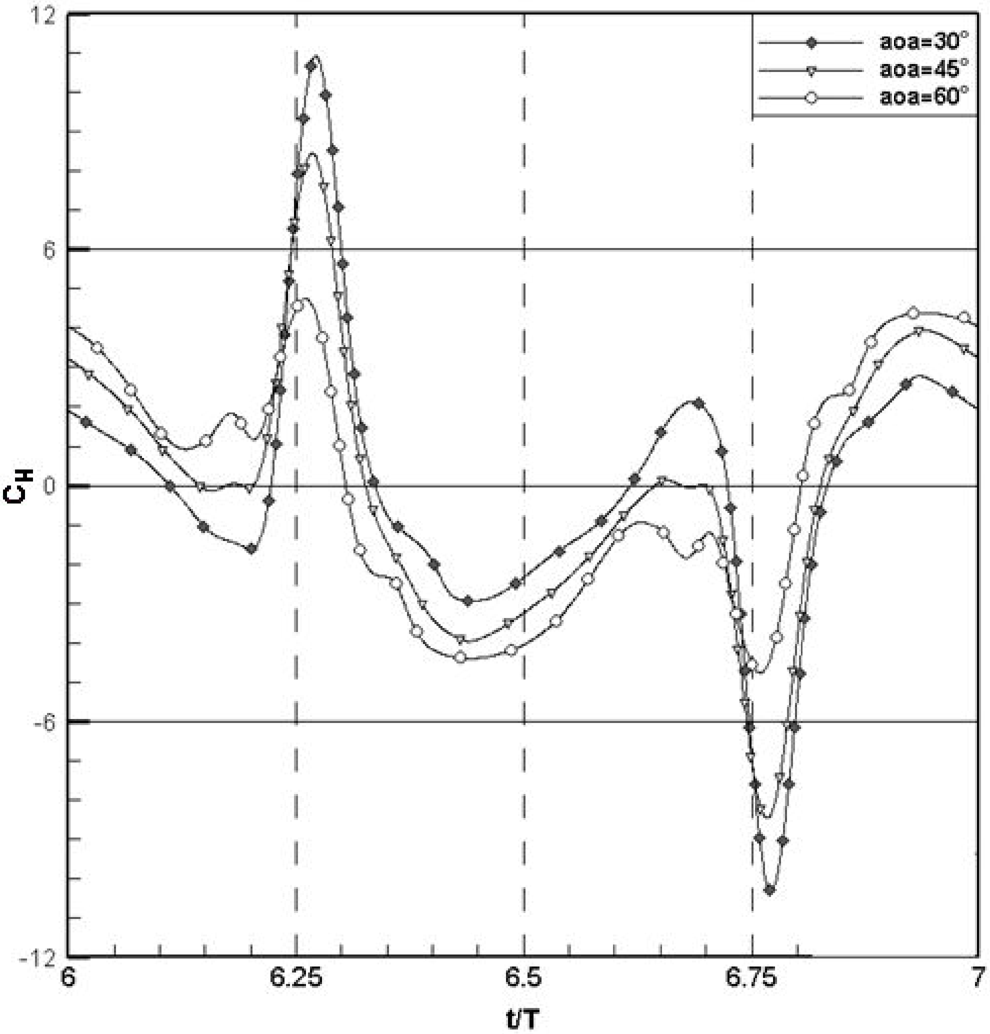

Figure 4.11 Horizontal force coefficients of NACA 0012 for B=2c and Re=1000 at 7th period

When focused on the horizontal force coefficient values in Figure 4.11, it is possible to say that same mechanism plays an active role in obtaining the maximum coefficient values for the rotational phase. For the translational phase of the motion, relatively massive leading and trailing edge vortices placed on the opposite side of the motion decreases the horizontal force coefficient which means increased dragging force for the 2nd region of the motion.

4.3 Effects of Reynolds Number

Reynolds number effect is analyzed for two different amplitudes, B=0 and 2c, at angle of attack of 45° for NACA 0012 profile but only the results of case where B=2c is given for brevity. The calculations have been performed for Re=200, 1000 and 5000 cases. The force coefficients are non-dimensionalized with respect to the maximum velocity corresponding to each Re number. It is found that in this regime of Reynolds number the force coefficients are affected slightly.

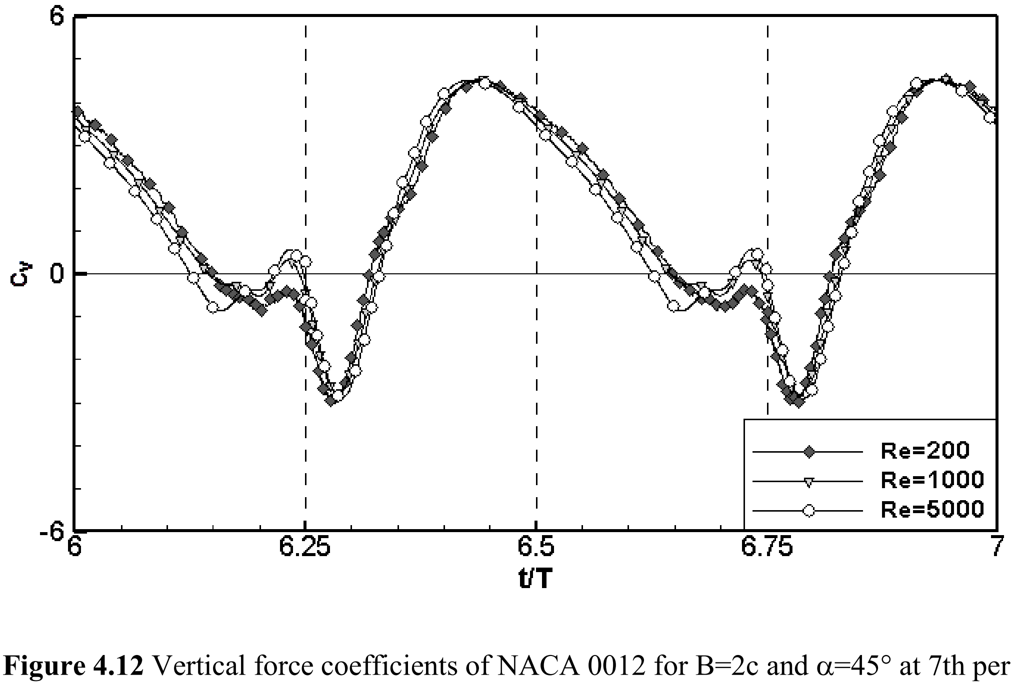

Figure 4.12 Vertical force coefficients of NACA 0012 for B=2c and α=45° at 7th period

As can be seen from Figure 4.12, the results for Reynolds numbers of 200, 1000 and 5000 are close to each other. Both in rotational and translational phases there are slight differences in vertical force coefficient values. When horizontal force coefficients are analyzed for the same case (Figure 4.13), slight differences are observed only in the rotational phase.

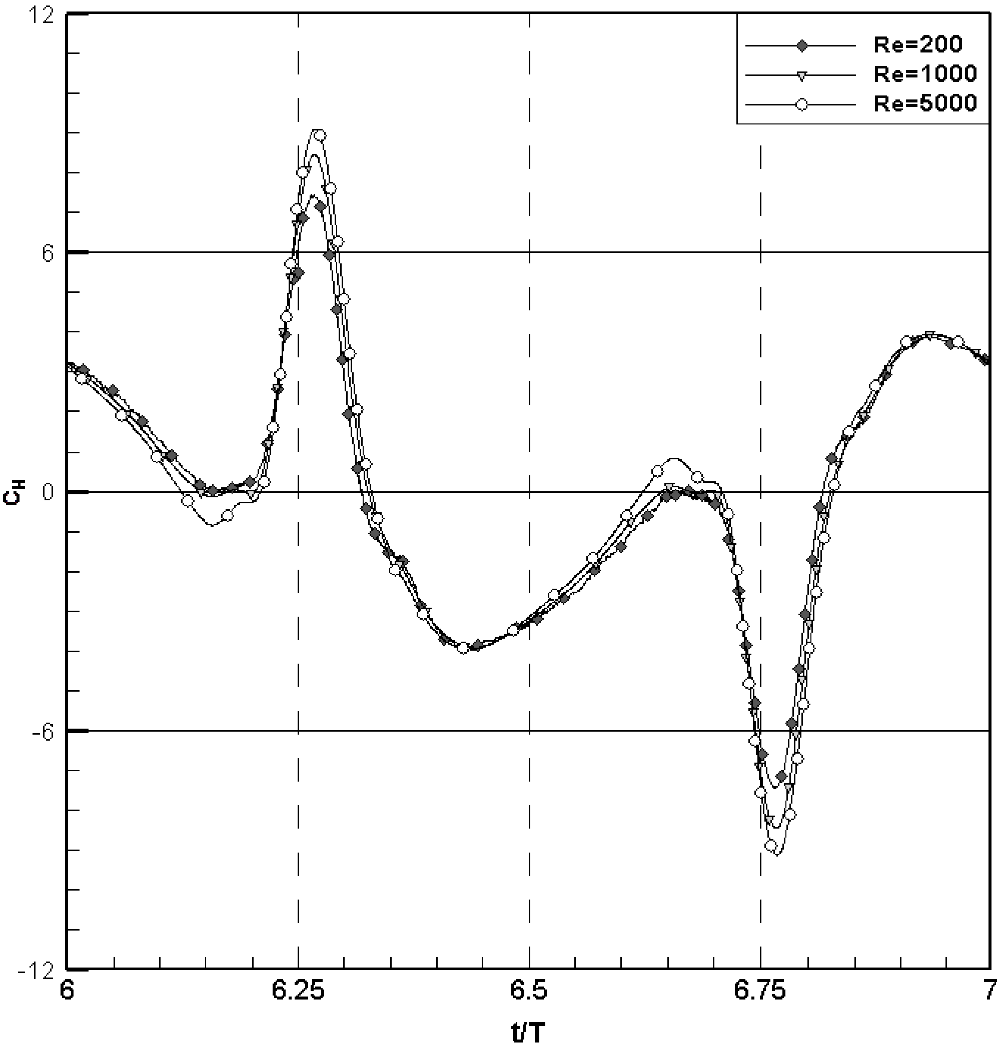

Figure 4.13 Horizontal force coefficients of NACA 0012 for B=2c and α=45° at 7th period

Table 4-2 Average aerodynamic values at different Reynolds numbers for α=45°

	B=0			B=2c		
	Re=200	Re=1000	Re=5000	Re=200	Re=1000	Re=5000
$\overline{C}_V$	0,932	0,919	0,979	1,412	1,505	1,315
$\overline{C}_H$	1,184	1,066	1,102	1,204	1,051	0,752
$\overline{V}(N)$	0,012	0,012	0,013	0,018	0,019	0,017
$\overline{H}(N)$	0,015	0,014	0,014	0,016	0,014	0,010
$\overline{V}/\overline{H}$	0,787	0,863	0,888	1,173	1,432	1,745

The mean force coefficients for different Reynolds numbers are represented in Table 4-2. Increase in Reynolds number values results in higher vertical to horizontal force proportion values. On the other hand, increase in Reynolds number causes higher energy consumption, which leads to inefficiency in terms of proportion of vertical to horizontal force values.

4.4 Effects of Airfoil Profile Shape-Camber

Two different airfoil profiles, namely NACA 0012 and NACA 6412, are used to investigate the effect of camber. The vertical and horizontal force coefficient values for these airfoils are compared over one non-dimensionalized period. The computational domain is kept nearly the same for both airfoil profiles. The numerical simulation of flapping motion for the symmetric and cambered profiles is performed for three different angles of attack and for five different amplitudes of motion in y-direction effect. For the ease of demonstration, only the results of computations at 60° are presented below.

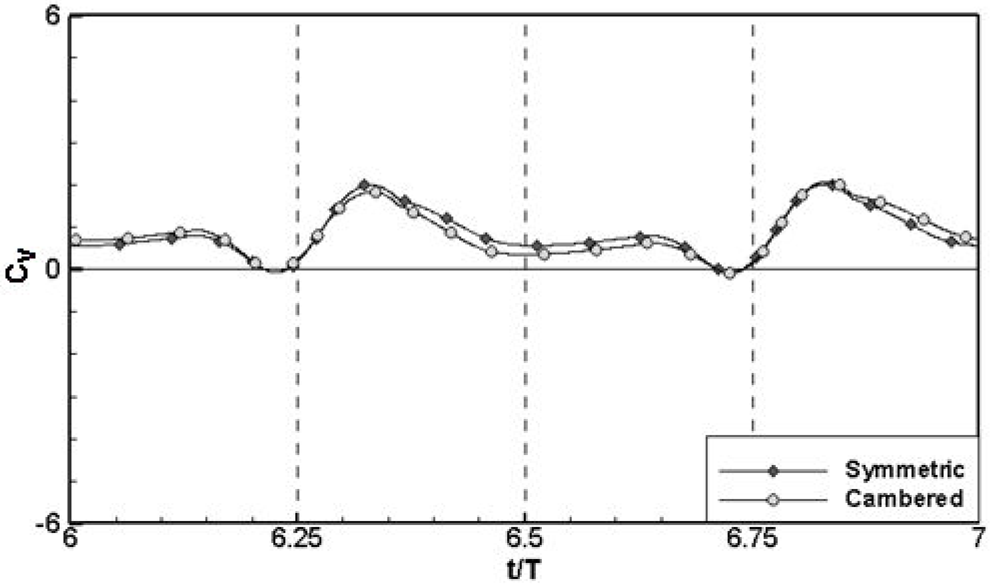

Figure 4.14 Vertical force coefficients of different profiles for B=0, α=60° and Re=1000 at 7th period

In Figure 4.14, the effect of camber is compared in terms of the vertical force coefficient variations at α=60°. The positive peak values of vertical force coefficients are higher for the symmetric profile in downstroke (between 6.25 and 6.75 non-dimensional time values) whereas that of horizontal force coefficients are higher for cambered one in upstroke. In downstroke lower surface of the cambered airfoil becomes the upper surface. This creates additional pressure increment on the suction side of the airfoil and results in lower vertical force coefficient values.

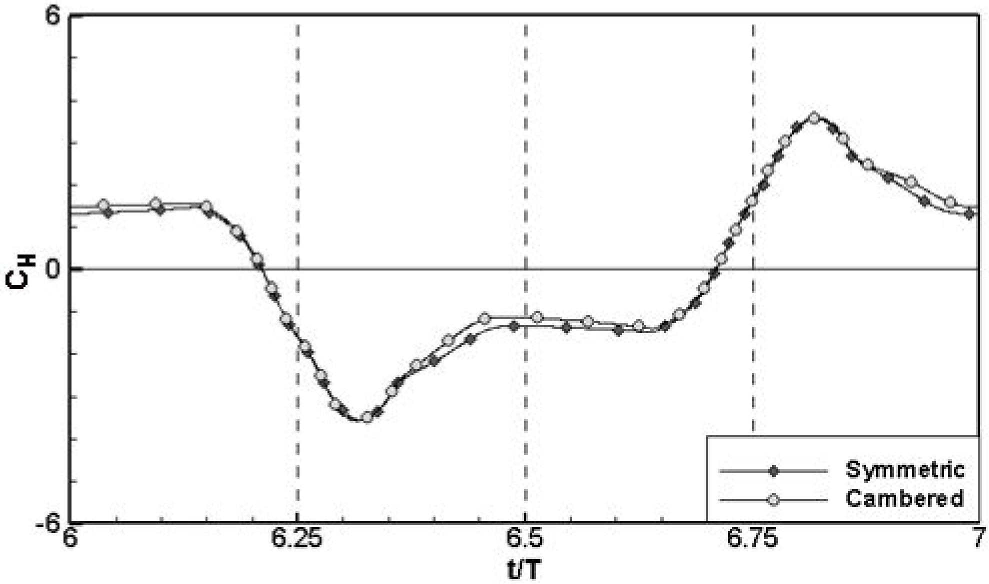

Figure 4.15 Horizontal force coefficients of different profiles for B=0, α=60° and Re=1000 at 7th period

Figure 4.15 shows the horizontal force coefficient values of NACA 0012 and NACA 6412 profiles. In downstroke the suction side of the cambered profile creates higher pressure fields, which brings about a decrease in horizontal force coefficient values, as expected. Aerodynamic force coefficient values of cambered airfoil do not differ much from that of the symmetrical airfoil case especially both in vertical and horizontal force coefficient variation.

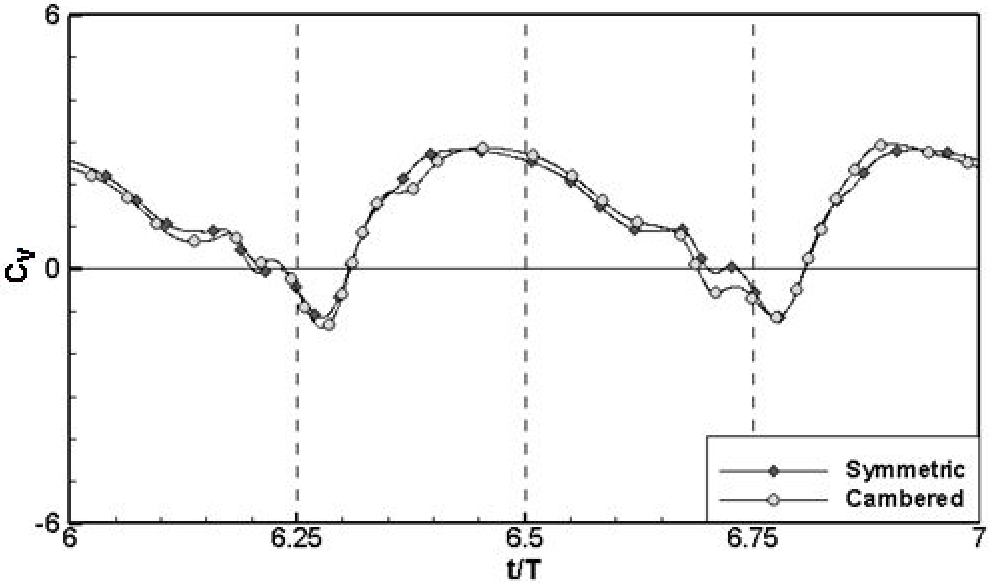

Figure 4.16 Vertical force coefficients of different profiles for B=2c, α=60° and Re=1000 at 7th period

The interpretations for the case B=0 can be made for the aerodynamic force coefficients of the case where B=2c (Figure 4.16 and Figure 4.17). The effect of camber on horizontal force coefficient can most easily be seen when the airfoil is in the rotational phase of the motion.

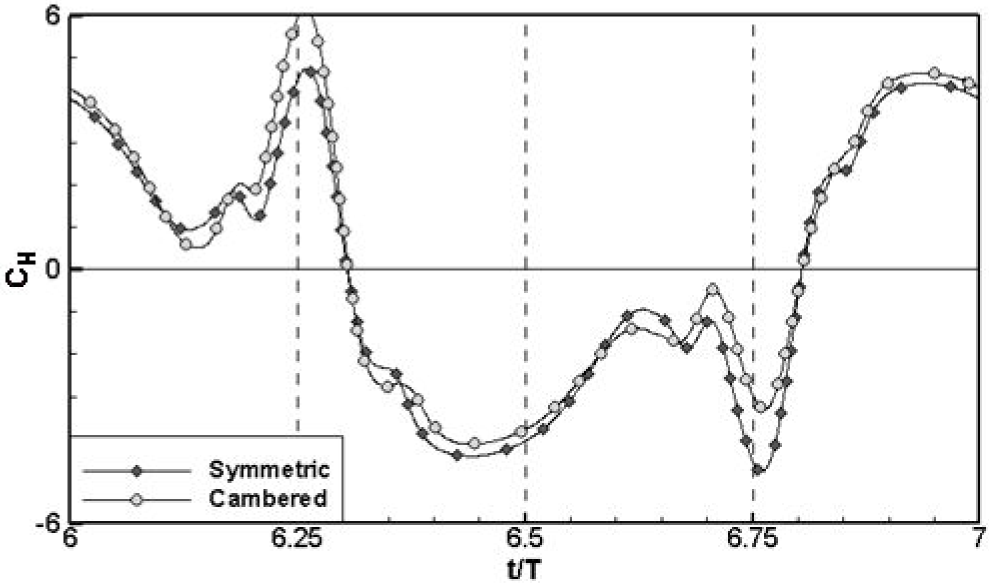

Figure 4.17 Horizontal force coefficients of different profiles for B=2c, α=60° and Re=1000 at 7th period

4.5 Average Aerodynamic Forces and Force Coefficients

Average aerodynamic force coefficient values are calculated for Reynolds number 1000 at 7th period of the numerical simulation. Table 4.3 includes totally 30 cases, parameters of which are tabulated in Table 4.1.

Table 4-3 Average aerodynamic force and force coefficient values at Re=1000

		B=0			**B = 0.5 C**			**B = 1C**			**B = 1.5 C**			**B = 2 C**		
		30°	**45°**	**60°**	**30°**	**45°**	**60°**	**30°**	**45°**	**60°**	**30°**	**45°**	**60°**	**30°**	**45°**	**60°**
NACA 0012	$\overline{C}_V$	0,784	0,919	0,861	0,875	0,986	0,882	1,010	1,167	0,948	1,129	1,306	1,095	0,997	1,505	1,370
	$\overline{C}_H$	0,622	1,066	1,613	0,595	1,056	1,516	0,502	1,136	1,582	0,296	1,093	1,747	-0,127	1,051	2,160
	$\overline{V}(N)$	0,010	0,012	0,011	0,011	0,013	0,011	0,013	0,015	0,012	0,015	0,017	0,014	0,013	0,019	0,018
	$\overline{H}(N)$	0,008	0,014	0,021	0,008	0,014	0,020	0,007	0,015	0,020	0,004	0,014	0,023	-0,002	0,014	0,028
	$\overline{V}/\overline{H}$	1,261	0,863	0,534	1,469	0,933	0,582	2,013	1,027	0,599	3,811	1,195	0,627	-7,844	1,432	0,634
NACA 6412	$\overline{C}_V$	0,791	0,882	0,834	0,831	0,970	0,865	0,980	1,125	0,925	1,090	1,265	1,072	0,949	1,458	1,329
	$\overline{C}_H$	0,650	1,080	1,608	0,582	1,050	1,509	0,507	1,114	1,567	0,322	1,089	1,749	-0,059	1,081	2,170
	$\overline{V}(N)$	0,010	0,011	0,011	0,011	0,013	0,011	0,013	0,015	0,012	0,014	0,016	0,014	0,012	0,019	0,017
	$\overline{H}(N)$	0,008	0,014	0,021	0,008	0,014	0,020	0,007	0,014	0,020	0,004	0,014	0,023	-0,001	0,014	0,028
	$\overline{V}/\overline{H}$	1,218	0,816	0,519	1,428	0,924	0,573	1,932	1,010	0,590	3,383	1,162	0,613	-15,986	1,349	0,612

It can be concluded that in order to obtain maximum average total force the most important parameter for the flapping motion studies is the amplitude of motion in y-direction. As the amplitude increases, average vertical force values obtained during the whole period of the motion also increases. When the effect of angle of attack is observed, which is the second important parameter, the biggest average vertical force coefficient values are obtained for 45° angle of attacks and total force coefficients are bigger for 60° angle of attack. The average horizontal force coefficient is quite large for 60° angle of attack which contributes significantly to the total force coefficient. But increase in the amplitude in y-direction results in lower average horizontal force coefficient values.

CHAPTER 5

EXPERIMENTAL RESULTS

Time dependent velocity fields were acquired by using the Particle Image Velocimetry technique for linear flapping motion. Obtained experimental results were used to validate the numerical results and investigate the basic vortex formation mechanism for the linear flapping motion. It was not possible for us to investigate the effects of vertical distance for the figure-of-eight motion since at its present configuration the experimental setup is not capable of performing any vertical movement in y-direction as stated in the previous chapter.

PIV measurements were performed for two different airfoils; NACA 0012 and NACA 6412, and for three different initial angles of attack; 30^0, 45^0, 60^0. For each experimental case, the whole period of the flapping motion is represented with 12 images recorded by two side-by-side positioned cameras.

In Figure 5.1 and Figure 5.2, experimental results are compared with the numerical results in terms of vortical structures. In Figure 5.1, the first half period of the linear flapping motion is represented with six images recorded by the first camera; whereas, in Figure 5.2 other half period is represented by the images recorded by the second camera. The linear flapping motion is symmetric, which means that the images recorded by the second camera are the mirror images of those recorded by the first camera. The motion of the airfoil in the figures below can be explained as follows; the airfoil translates in the horizontal direction at the initial angle of attack setting and at t=0.163T (for the other half-period of the motion t=0.663T), it starts to rotate around its quarter chord. At the non-dimensional time step of 0.211T (0.711T), it is approximately in the middle of its rotation and as anticipated it reaches the maximum angle of attack at t=0.25T (t=0.75T). Then it starts to translate and rotate in the opposite direction which is evident in the image corresponding to t=0.298T (t=0.298T). It proceeds to rotate until it reaches its initial angle of attack at t=0.349T (0.849T). Then it translates with a constant angle of attack in the horizontal direction at t=0.433T (0.933T).

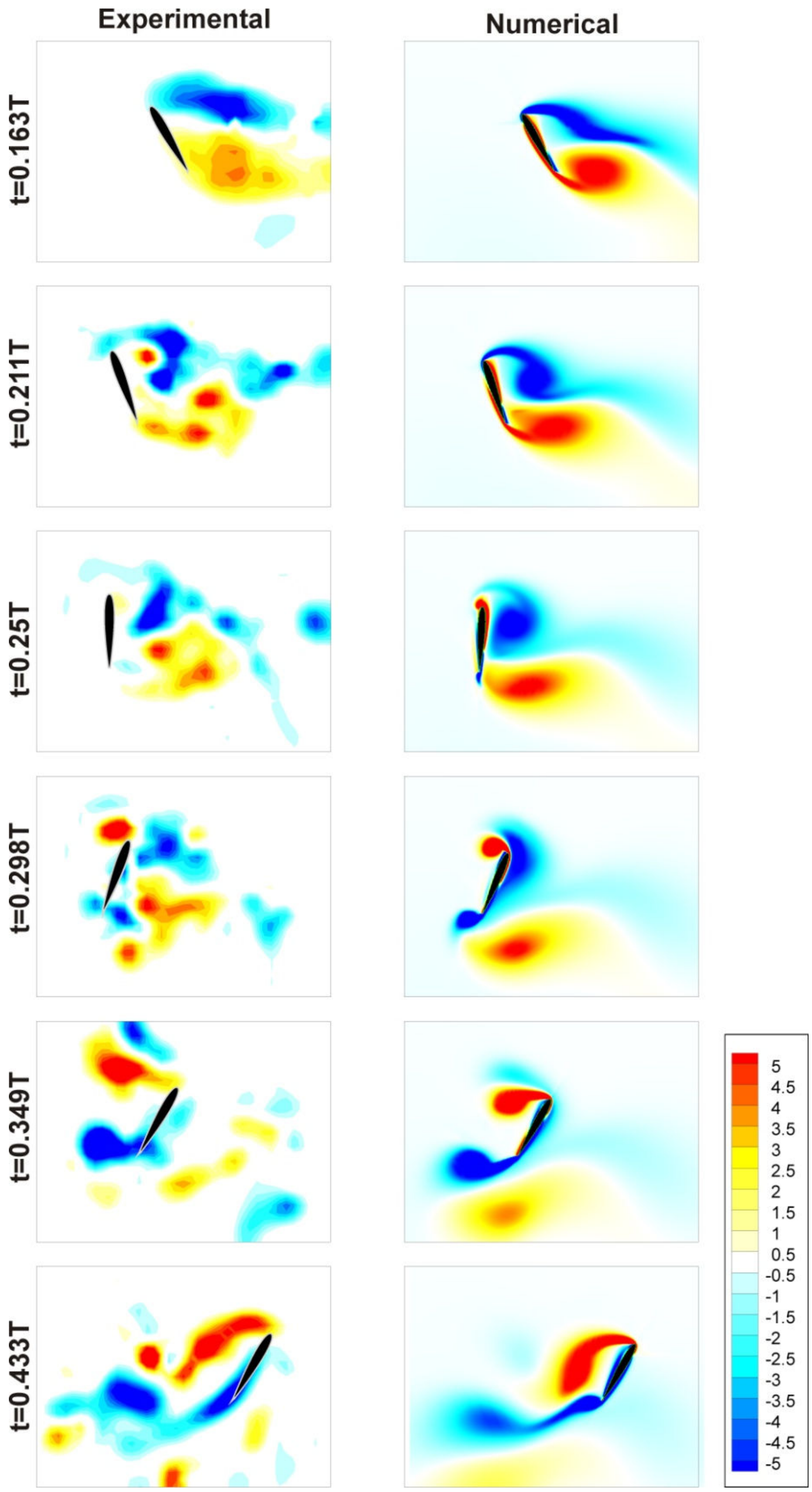

Figure 5.1 Non-dimensional vorticity contours derived from experimental and numerical results of NACA 0012 airfoil for $\alpha_0=60^0$ (Camera 1)

Needless to say, that the experimental results are in fair accordance with the numerical ones in terms of vortical structures. Numerically acquired formation of leading and trailing edge vortices and their interactions are also validated with the results of PIV experiments.

For the second half-period of the motion, vortex formation mechanism of the linear-flapping motion case can be explained as follows; massive leading and trailing edge vortices move with the airfoil during the translational phase (t= 0.663T). Then with the rotation of the airfoil, leading and trailing edge vortices curls towards the airfoil in the suction side (t=0.711T). When the airfoil reaches its maximum angle of attack value which corresponds to 90^0, leading and trailing edge vortices are placed at the side towards which airfoil starts its translational motion. When the airfoil moves on the opposite direction, recently formed leading and trailing edge vortices interact with ones from the previous phase (t=0.798T and t=0.849T). The interaction between counter-rotating vortices results in vorticity destruction which is an undesired condition in terms of lift production.

Non-dimensional vorticity contours derived from the experimental and numerical results for the other cases are presented in A.1.

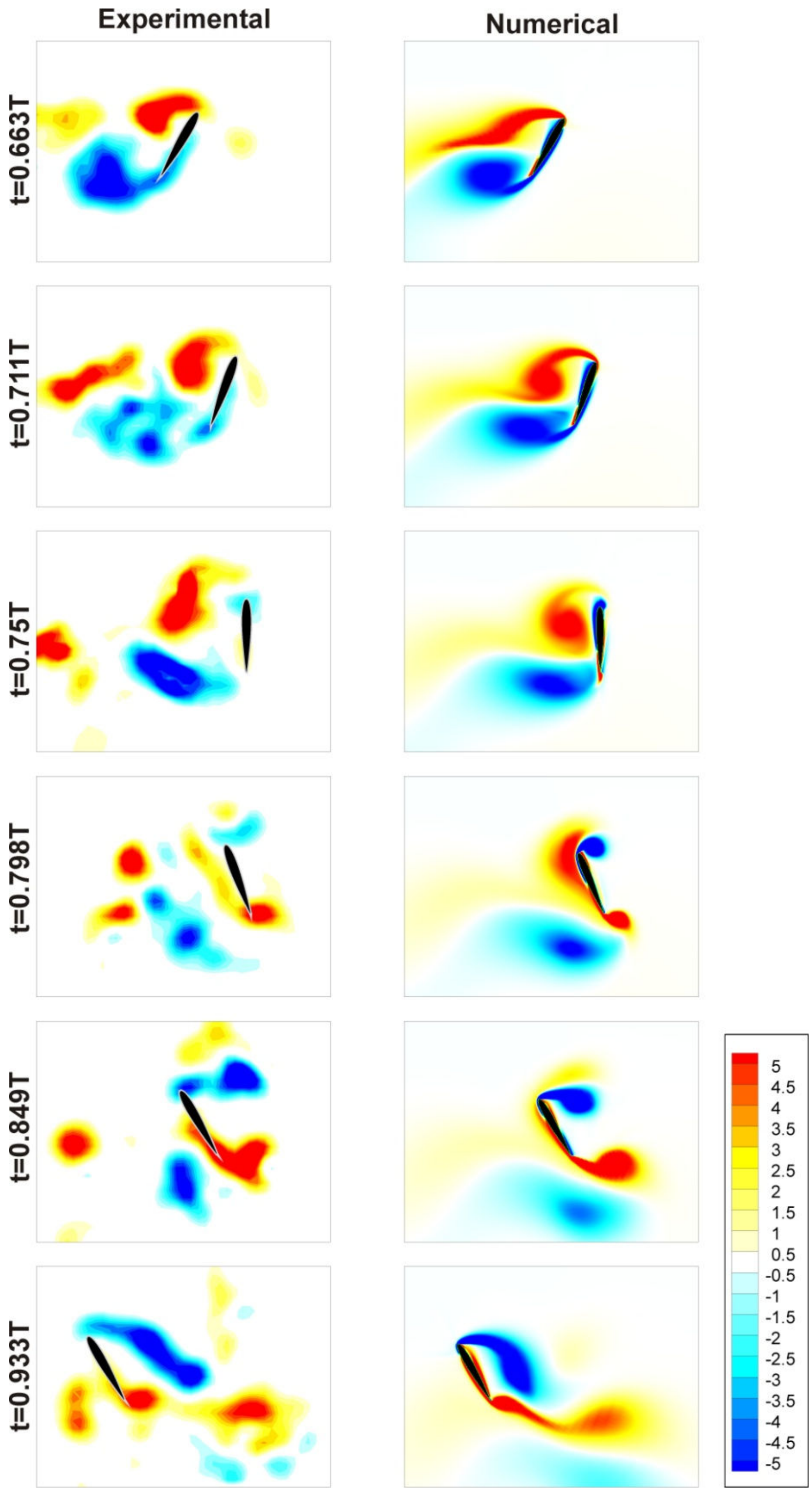

Figure 5.2 Non-dimensional vorticity contours derived from experimental and numerical results of NACA 0012 airfoil for $\alpha_0=60^0$ (Camera 2)

CHAPTER 6

CONCLUSION

In this study, a detailed numerical investigation is performed in order to investigate the effect of motion in y-direction as well as other important parameters of flapping motion, such as the Reynolds number, initial angle of attack and the geometry (camber) on aerodynamic force coefficients and vortex formation mechanisms at low Reynolds number regime. The kinematics of motion is described for two different trajectories: linear and figure-of-eight flapping motions in hover.

The tools used for these investigations are two-fold: the numerical solution techniques using CFD and the experimental measurements using the PIV techniques. The numerical simulations are performed using a commercial CFD package Fluent with moving grid capability. User Defined Functions are used to move the grid generated around the airfoils. The flow field for flapping hover flight is investigated for symmetrical and cambered airfoil profiles both having chord lengths of 0.01m for numerical computations. Computed aerodynamic force coefficients are compared for these profiles having different angles of attack and Reynolds number. Later on, Particle Image Velocimetry (PIV) technique is used for validation of the numerical results and analysis of the basic vortex formation mechanisms only for the linear flapping motion. Investigation of the motion in y-direction for the figure-of-eight motion could not be achieved since at its present configuration the experimental set is not capable to perform any vertical movement in y-direction as stated previously.

At first numerical tests are carried out on the NACA 0012 airfoil to analyze time step and grid size effect on the aerodynamic force coefficient values. Previous work done by Kurtuluş [3] is considered as benchmark to verify grid size and time step. Then, by using the verified grid size and time step, numerical simulations are performed. The vortex formation, interaction of the leading and trailing edge vortices are represented with vorticity contours.

The shedding of the vortices especially which are coming from the leading edge have different mechanisms for different amplitudes in y-direction (B) and initial angle of attack parameters, so the aerodynamic force coefficients are mostly influenced by the effect of these parameters.

Comparison between figure-of-eight and linear flapping motion reveals that relatively massive leading and trailing edge vortices are generated in figure-of-eight motion. Larger vortical structures are formed in the case where B=2c. Moreover, as the recently generated leading and trailing edge vortices do not interact with the vortices formed in the previous stroke, they maintain their strength for a longer time when compared to linear flapping motion.

In addition to that, for the figure-of-eight motion case airfoil moves in a more continuous manner and its vertical movement becomes beneficial in terms of increasing the strength of trailing edge vortex as a result of the interaction between co-rotating leading edge vortex, that is formed during the vertical motion, and the trailing edge vortex that is recently formed at the beginning of downstroke.

Investigation of effect of initial angle of attack brings out that lower initial angle of attack values, i.e. higher rotational velocities, result in lower lift coefficient values at the end of the rotational phase and higher values at the beginning of the rotational phase. It is obvious that there is no negative lift region for B=0 cases. When t/T is 6.25 and 6.75, the amplitude of these peaks becomes zero as a result of the 90° angle of attack the airfoil makes with the horizontal axis. It is observed that for 60° angle of attack, although the maximum lift coefficient value is bigger than all other cases, in translational region the lift coefficient value drops abruptly. The effect of parameters such as Reynolds number and camber is also investigated but the results shows that these parameters do not have significant effects on aerodynamic forces and vortical structures.

The experimental results are in accordance with the numerical ones in terms of vortical structures. Numerically acquired formation of leading and trailing edge vortices and their interactions are also validated with the results of PIV experiments.

In the experimental setup, cameras were mounted on a stationary platform although the wing profile was moving. This situation brought about that the perspective view of the wing was captured at some locations of the moving profile, which results in shadow regions on the surfaces of the wing. As a consequence, at these locations flow field close to the surfaces of the airfoil could not be analyzed successfully, which may be the reason of the detached vortices seen in the experimental results. Utilization of moving cameras in synchronization with the moving wing may be a solution for this problem. In addition to this, since the leading and trailing edges of the wing profile does not allow the laser light to illuminate both sides and reflects the laser light irregularly, this also causes shadow regions in the flow field. This problem can be solved by using an appropriate mirror.

The validation of the present computational results with the experimental results encourages us to conclude that the present numerical method can be a reliable alternative to experimental techniques. The results obtained from the present numerical investigations provided good description of the unsteady aerodynamic mechanisms for the generation of lift and drag during the flapping motion in hover.

The experimental results are obtained for linear type of flapping motion. This is due to the fact that at its present configuration the experimental set is designed to perform only the linear prescribed motion in the x-direction and no y motion capability is available. However, a new experimental set-up is under construction to incorporate a two dimensional motion, with which it will be possible to translate the wing along both the x and y axis. With this new configuration it will be possible to perform any kind of flapping motion such as the figure of eight motion. The new system will be driven by means of servo motors instead of currently used step motors and therefore it will be much easier to program the new traversing system for the specified motion kinematics [59]. With this new system it will be also possible to measure the torque generated by each of the servo motors which will be an indication of the forces generated by the flapping motion. Yet, it will not be possible to measure the exact forces acting on the airfoil during the flapping motion. With these servo motors one can have an idea about the magnitude of the forces acting on the airfoil during a period of flapping oscillation. The next step in our experimental investigations will be to incorporate an internal strain gage balance inside the wing and to measure the instantaneous forces and moments acting on the flapping wing.

As a future work, efficiencies of linear and figure of eight motion in hover can be computed in terms of the acquired vertical force, which is the force opposing to the weight, reference velocity and the energy consumed to achieve these motions. In addition to this, when the motion of the wings of biological flyers are investigated, it can be seen that the shape of the wings are changing, i.e. camber, twist angle, angle of attack is changing at different phases of the wing stroke. In order to simulate this kind of motion, deformable grids can be used in numerical studies.

REFERENCES

[1] Young, J., *Numerical Simulation of the Unsteady Aerodynamics of Flapping Airfoils*, PhD Thesis, The University of New South Wales, Sydney, 2005.

[2] Wang, Z. J., *Vortex Shedding and Frequency Selection in Flapping Flight, Journal of Fluid Mechanics*, Vol. 410, pp. 323-341, 2000.

[3] Kurtulus, D. F., *Numerical and Experimental Analysis of Flapping Motion in Hover: Application to Micro Air Vehicle,* Joint Ph.D. thesis Poitiers University/ENSMA (Poitiers France) and METU (Ankara-Turkey), Poitiers, France, 17 June 2005.

[4] Sarıgöl, E., *Experimental and numerical analysis of flapping wing motion*, Ph.D. Dissertation, METU Aerospace Engineering Department, July 2007.

[5] Weis-Fogh, T. and Jensen, M., *Biology and physics of locust flight: I. Basic principles in insect flight: A critical review*, Philosophical Transactions of the Royal Society of London, Series B 239, 415–58, 1957.

[6] Sane, S. P. and Dickinson, M. H., *The aerodynamic effects of wing rotation and a revised quasi-steady model of flapping flight*, Journal of Experimental Biology 205, 1087– 96, 2002.

[7] Ellington, C. P., *The aerodynamics of hovering insect flight: I. The quasi-steady analysis*, Philosophical Transactions of the Royal Society of London, Series B 305, 1–15, 1984.

[8] Ellington, C. P., *Morphological parameters, II: The aerodynamics of hovering insect flight*, Philosophical Transactions of the Royal Society of London, Series B 305, 17–40, 1984.

[9] Ellington, C. P., *The aerodynamics of insect flight: III. Kinematics*, Philosophical Transactions of the Royal Society of London, Series B 305, 41–78, 1984.

[10] Ellington, C. P., *The aerodynamics of hovering insect flight: IV. Aerodynamic mechanisms*, Philosophical Transactions of the Royal Society of London, Series B 305, 79–113, 1984.

[11] Ellington, C. P., *The aerodynamics of hovering insect flight: V. A Vortex theory*, Philosophical Transactions of the Royal Society of London, Series B 305, 115–44, 1984.

[12] Ellington, C. P., *The aerodynamics of hovering insect flight: VI. Lift and Power Requirements*, Philosophical Transactions of the Royal Society of London, Series B 305, 145–181, 1984.

[13] Shyy, W., Lian, Y., Tang, J., Viieru, D., Liu, H*., Aerodynamics of Low Reynolds Number Flyers*, Cambridge University Press, 2008.

[14] Dickinson, M.H. and Götz, K., *Unsteady Aerodynamic Performance of Model Wings at Low Reynolds Numbers*, J. Exp. Biol., 174, pp.45-64, 1993

[15] Ellington, C. P., Van den Berg, C., Willmott, A. P., and Thomas, A. L. R., *Leading-edge vortices in insect flight*, Nature (London) 384, 626–30, 1996.

[16] http://scienceblogs.com/grrlscientist/2007/02/gyroscopes_tell_moth_how_to_fl.php, Last accessed:27.08.2009

[17] Van Den Berg, C. and Ellington, C.P., *The three-dimensional leading-edge vortex of a 'hovering' model hawkmoth*, Phil. Trans. R. Soc. Lond. B 352, pp.329-340, 1997

[18] Van Den Berg, C. and Ellington, C.P., *The vortex wake of a 'hovering' model hawkmoth*, Phil. Trans. R. Soc. Lond. B 352, pp.317-328, 1997

[19] Dickinson, M. H., Lehmann, F.-O., and Sane, S. P., *Wing rotation and the aerodynamic basis of insect flight*, Science 284, 1954–60, 1999.

[20] http://www.lightblog.com/member/premenopaws/?xjMsgID=23934, Last accessed: 27.08.2009

[21] Birch, J. M. and Dickinson, M. H., *Spanwise flow and the attachment of the leading-edge vortex on insect wings*, Nature (London) 412, 729–33, 2001.

[22] Usherwood, J.R. and Ellington, C.P., *The Aerodynamics of revolving wings: I Model Hawkmoth wings*, J. Exp. Biol., 205, pp.1547–1564, 2002.

[23] Birch, J.M., Dickson, W.B. and Dickinson, M.H., *Force production and flow structure of the leading edge vortex on flapping wings at high and low Reynolds numbers*, J. Exp. Biol., 207, pp.1063-1072, 2004.

[24] Lehmann, F.-O., Sane, S. P., and Dickinson, M. H., *The aerodynamic effects of wing–wing interaction in flapping insect wings*, Journal of Experimental Biology 208, 3075–92, 2005.

[25] Lu, Y., Shen, G.X. and Su, W.H., *Flow visualization of dragonfly hovering via electromechanical model*, AIAA Journal, Vol.45, No.3, pp. 615-623, 2007.

[26] http://flickr.com/photos/sakmd/1312205876/ , Last accessed: 27.08.2009

[27] Dickinson, M.H., Lehmann, F.O. and Götz, K.G., *The active control of wing rotation by Drosophila*, J. Exp. Biol. 182, pp.173-189, 1993.

[28] Willmott, A.P. and Ellington, C.P., *The Mechanics of Flight in the Hawkmoth Maduca Sexta I. Kinematics of Hovering and Forward Flight*, Exp. Biol., 200, pp.2705-2722, 1997.

[29] Willmott, A.P. and Ellington, C.P., *The Mechanics of Flight in the Hawkmoth Manduca Sexta II. Aerodynamic Consequences of Kinematic and Morphological Variation*, Exp. Biol., 200, pp.2723-2745, 1997.

[30] Srygley, R. B. and Thomas, A. L. R., *Unconventional lift-generating mechanisms in free-flying butterflies*, Nature (London) 420, 660–4, 2002.

[31] Fry, S. N., Sayaman, R., and Dickinson, M. H., *The aerodynamics of free-flight maneuvers in Drosophila*, Science 300, 495–8, 2003.

[32] Bomphrey, R. J., Lawson, N. J., Harding, N.J., Taylor, G.K., and Thomas, A.L.R., *The aerodynamics of Manduca sexta: digital particle image velocimetry analysis of the leading-edge vortex*, The Journal of Experimental Biology 208, pp.1079-1094, 2005.

[33] Warrick, D. R., Tobalske, B. W., and Powers, D. R., *Aerodynamics of the hovering hummingbird*, Nature (London) 435, 1094–7, 2005.

[34] http://latimesblogs.latimes.com/lanow/2008/04/living-the-high.html, Last accessed: 27.08.2009

[35] Ramamurti, R. and Sandberg, W.C., *A three-dimensional computational study of the aerodynamic mechanisms of insect flight*, J. Exp. Biol., 205, pp.1507-1518, 2002.

[36] Sun, M. and Tang, J., *Lift and power requirements of hovering flight in Drosophila virilis*, J. Exp. Biol., 205, pp.2413-2427, 2002

[37] Miller, L.A. and Peskin, C.S., *A computational fluid dynamics of 'clap and fling' in the smallest insects*, J. Exp. Biol., 208, pp.195-212, 2005.

[38] Miller, L.A. and Peskin, C.S., *When vortices stick: an aerodynamic transition in tiny insect flight*, J. Exp. Biol., 207, pp.3073-3088, 2004.

[39] Wu, J.H. and Sun, M., *Unsteady aerodynamic forces of a flapping wing*, J. Exp. Biol., 207, pp.1137-1150, 2004.

[40] Aono, H. and Liu, H., *Vortical Structures and Aerodynamics of Hawkmoth Hovering*, Journal of Biomechanical Science and Engineering, Vol. 1, No.1, pp.234-245, 2006

[41] Zuo, D., Peng, S., Chen, W. and Zhang, W., *Numerical simulation of flapping-wing insect hovering flight at unsteady flow*, Int. J. Numer. Meth. Fluids, 2006.

[42] http://wightrambler.blogspot.com/2009/06/dancing-with-death.html, Last accessed: 27.08.2009

[43] Sun, M. and Yu, X., *Aerodynamic force generation in hovering flight in a tiny insect*, AIAA Journal, Vol. 44, No.7, pp.1532-1540, 2006.

[44] http://www.biobest.be/v1/en/producten/nuttig/encarsia.htm, Last accessed: 27.08.2009

[45] Bos, F.M., Lentink, D., van Oudheusden, B.W and biji, H., *Numerical study of kinematic wing models of hovering insect flight*, 45th AIAA Aerospace Sciences Meeting and Exhibit, 8-11 January 2007, Reno-Nevada.

[46] Liu, H., *Computational Biological Fluid Dynamics: Digitizing and Visualizing Animal Swimming and Flying*, Integr. Comp. Biol., 42:1050–1059, 2002.

[47] Wang, Z.J., Birch, J.M. and Dickinson, M.H., *Unsteady forces and flows in low Reynolds number hovering flight: two-dimensional computations vs robotic wing experiments*, J. Exp.Biol., 207, pp.449-460, 2004.

[48] Wang, Z. J., *Two Dimensional Mechanism for Insect Hovering*, Physical Review Letters, Vol. 85, No. 10, September 2000.

[49] Wang, Z.J., *Computation of insect hovering*, Math. Meth. Appl. Sci. 2001; 24:1515–1521, 2001.

[50] Eldredge, J.D., *Efficient tools for the simulation of flapping wing flows*, 43rd AIAA Aerospace Sciences Meeting and Exhibit, 10*13 January Reno, Nevada, 2005.

[51] Kurtuluş D. F., Farcy A., Alemdaroglu N., *Unsteady Aerodynamics of Flapping Airfoil in Hovering Flight at Low Reynolds Numbers*, 43rd AIAA Aerospace Sciences Meeting and Exhibit, AIAA-2005-1356, Reno, Nevada, 10 - 13 Jan 2005.

[52] Akay B., *Unsteady Aerodynamic Calculations of Flapping Wing Motion*, M.Sc. thesis, METU Aerospace Engineering Department, September 2007.

[53] Başkan, Ö., Alemdaroğlu, N. and Sarıgöl, E., *Investigation of Flow around a Flapping Airfoil in Hover: Comparison of Linear and Figure-of-eight Motion,* 5th Ankara International Aerospace Conference, Ankara, Turkey, 2009.

[54] *Fluent User's Guide*, 2006.

[55] Bos, F. M., *Influence of Wing Kinematics on Performance in Insect Flight: a Numerical Investigation,* M.Sc. thesis, Delft University of Technology Aerodynamics Dept., 2005.

[56] Young, J., and Lai, J. C. S., *Vortex Lock-In Phenomenon in the Wake of a Plunging Airfoil*, AIAA Journal, Vol. 45, No. 2, 2007.

[57] Raffel, M., Willert, C., and Kompenhans, J., *Particle Image Velocimetry A Practical Guide*, Springer Verlag, Berlin, 1998.

[58] Dantec Dynamics, *Flow Manager Software and Introduction to PIV Instrumentation*, 5th Edition, 2000.

[59] Alemdaroğlu N., *TÜBİTAK Project Proposal (Project no: 109M311),* METU Aerospace Engineering Dept., Ankara, 2009.

APPENDIX A

COMPARISON OF VORTICITY CONTOURS

The comparison of PIV measurements and numerical results during a period at different time values are represented in Figures from A.1 to A.10. Left and right column of each figure represents experimental and numerical results, respectively. In the experimental part of the study there exist totally 6 cases analyzed one of which is presented in Chapter 6. Remaining 5 cases and their comparisons with numerical simulations are given below:

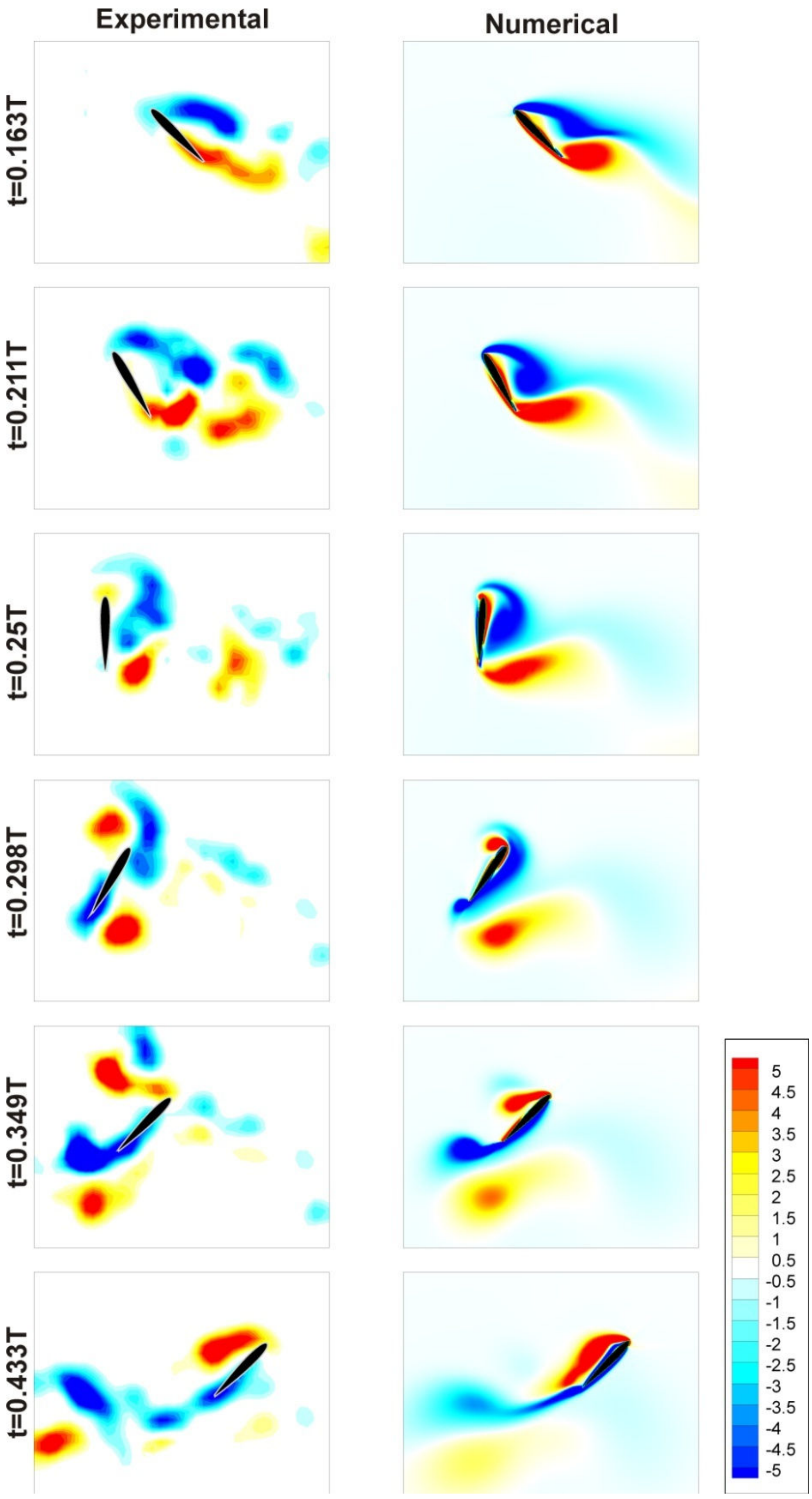

Figure A.1 Vorticity contours derived from experimental and numerical results for NACA 0012 airfoil at $\alpha_0=45^0$ (Camera 1)

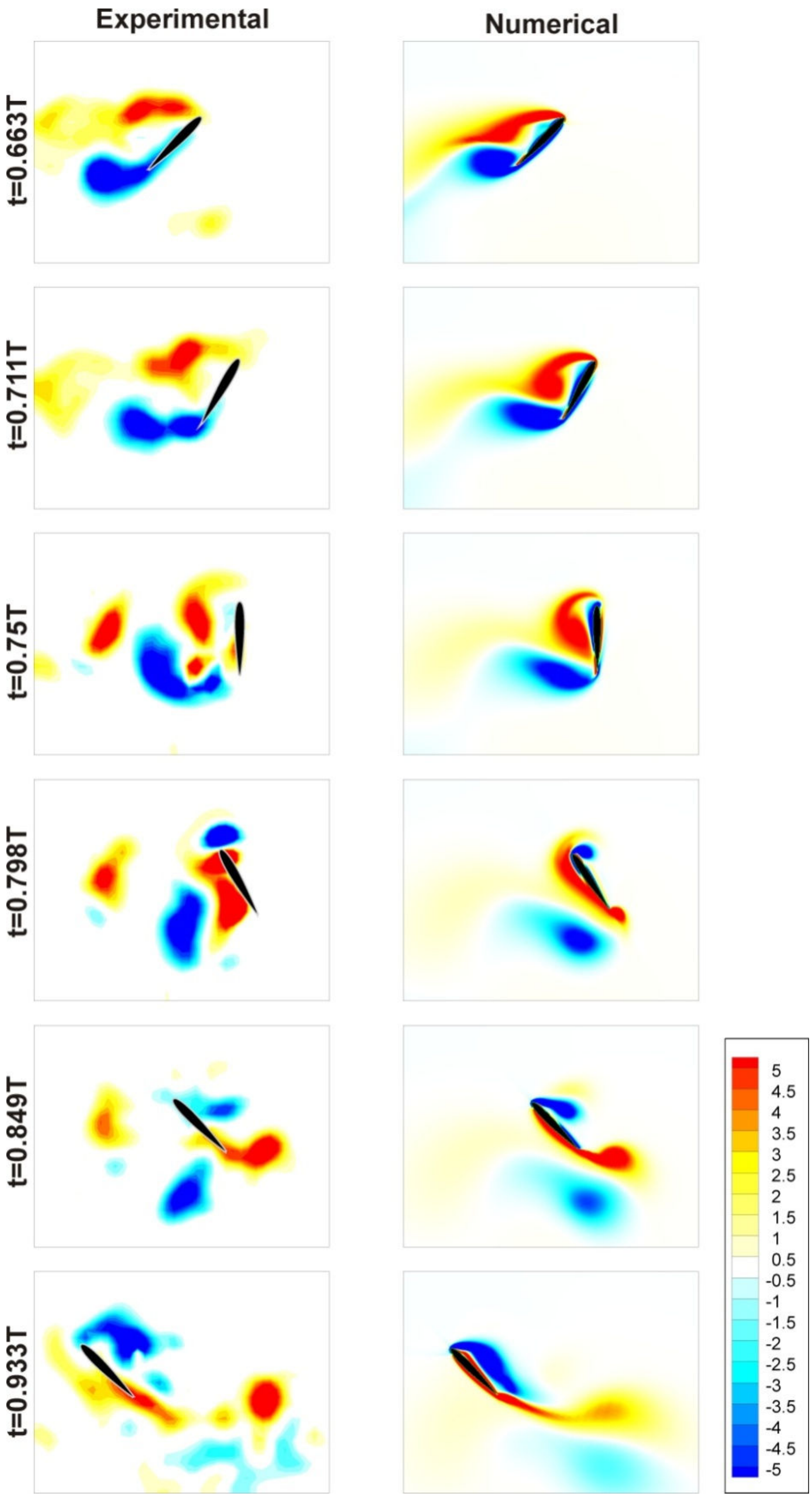

Figure A.2 Vorticity contours derived from experimental and numerical results for NACA 0012 airfoil at $\alpha_0=45^0$ (Camera 2)

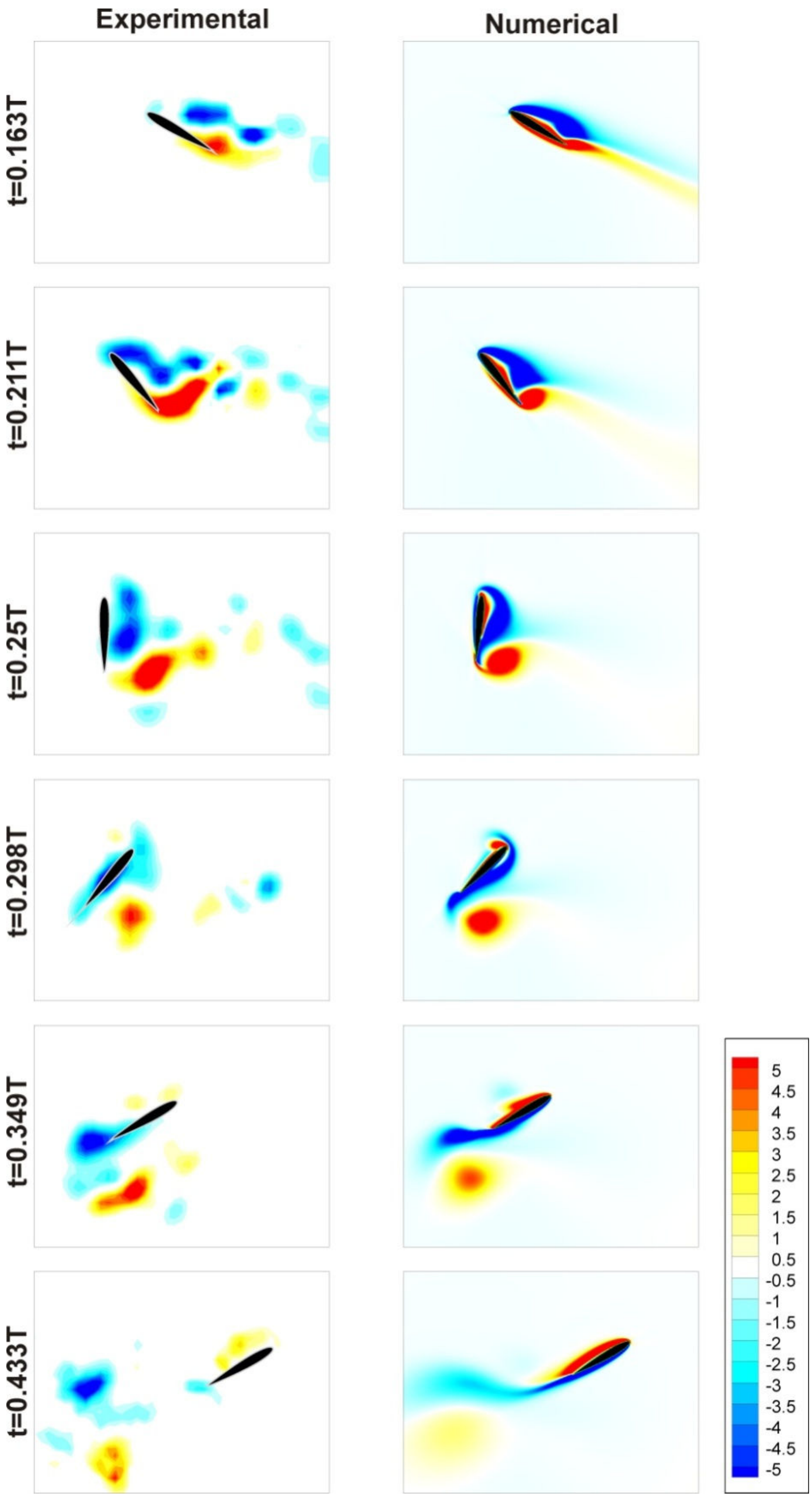

Figure A.3 Vorticity contours derived from experimental and numerical results for NACA 0012 airfoil at $\alpha_0=30^0$ (Camera 1)

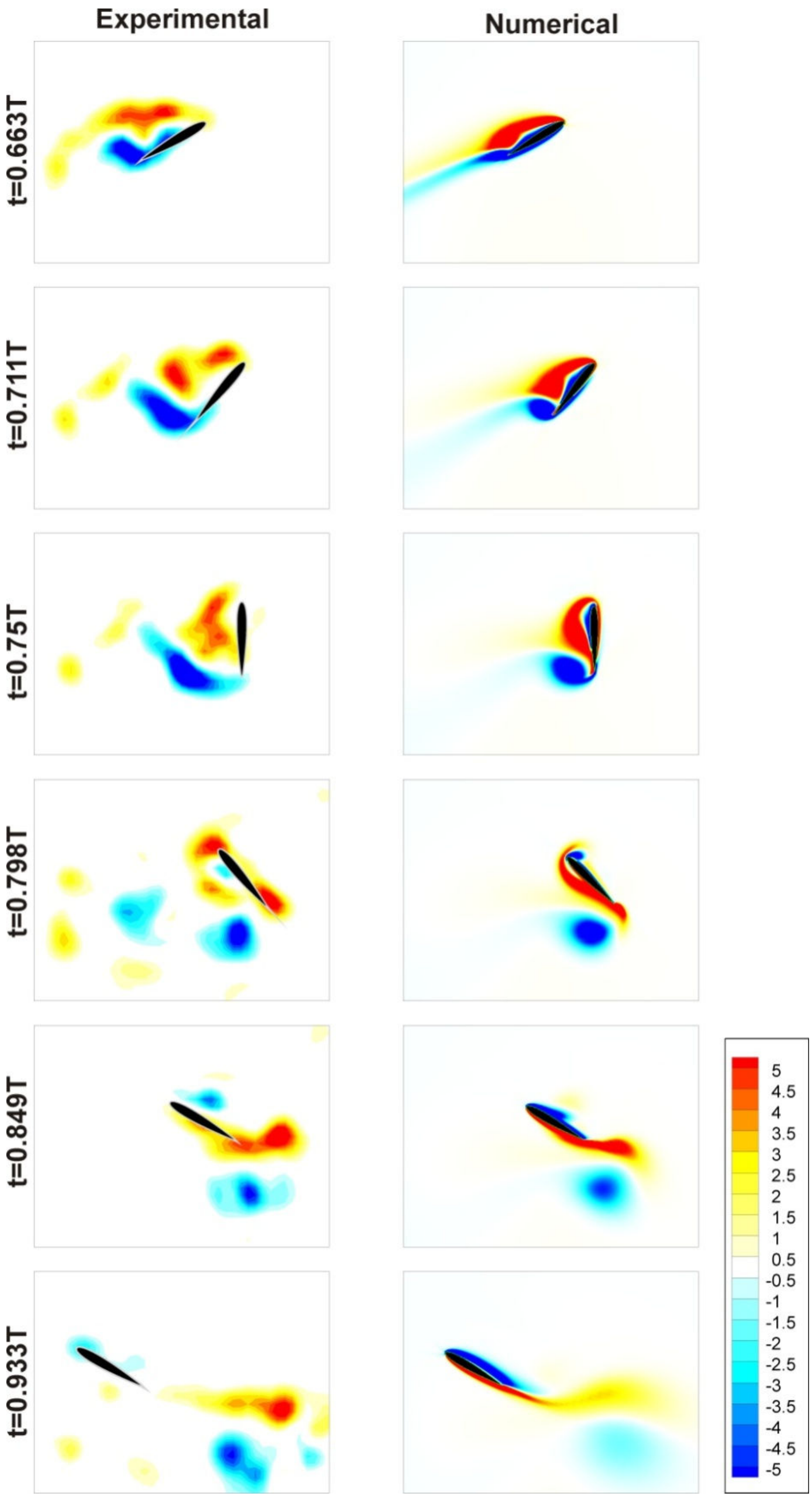

Figure A.4 Vorticity contours derived from experimental and numerical results for NACA 0012 airfoil at $\alpha_0=30^0$ (Camera 2)

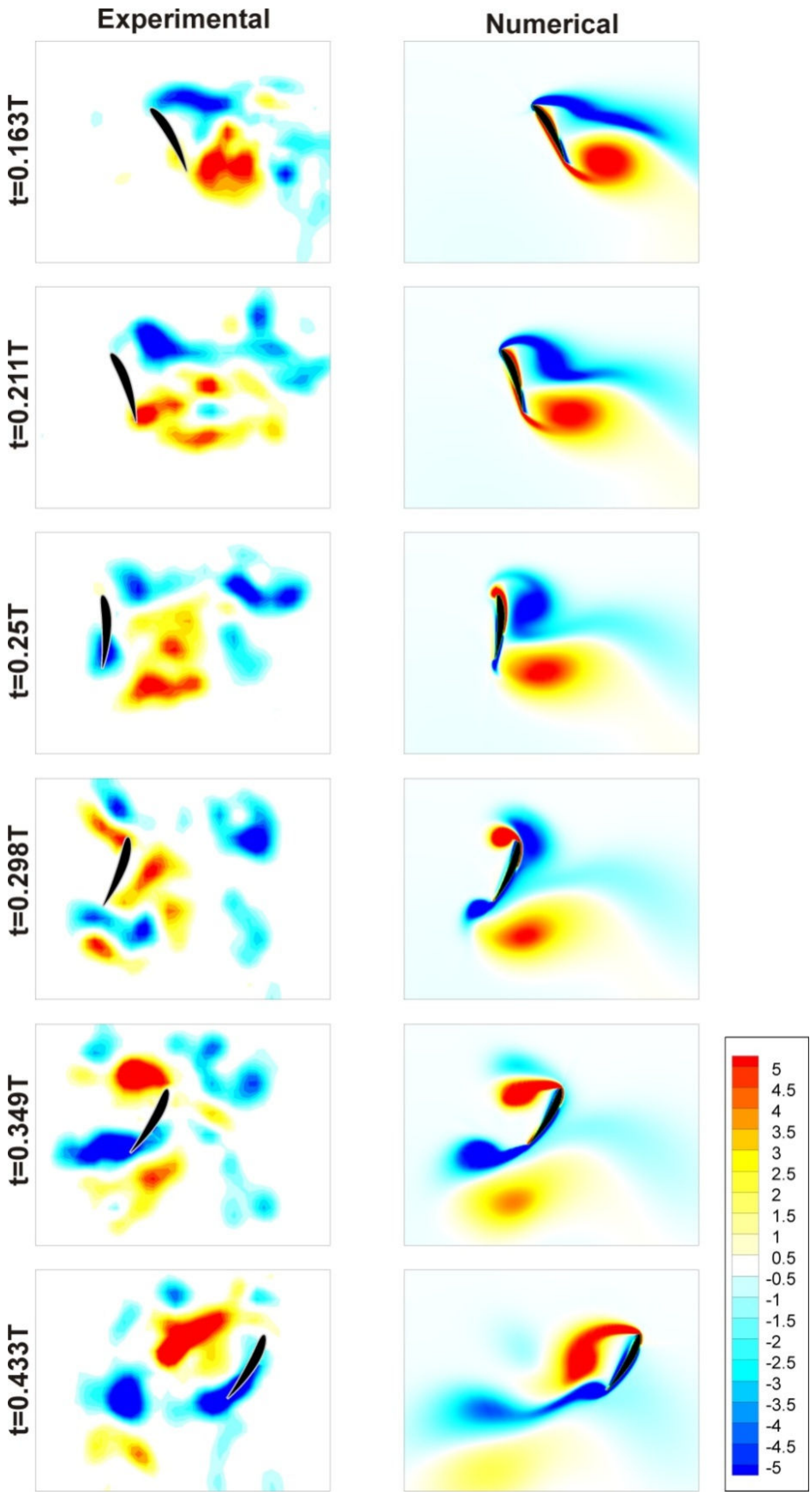

Figure A.5 Vorticity contours derived from experimental and numerical results for NACA 6412 airfoil at $\alpha_0=60^0$ (Camera 1)

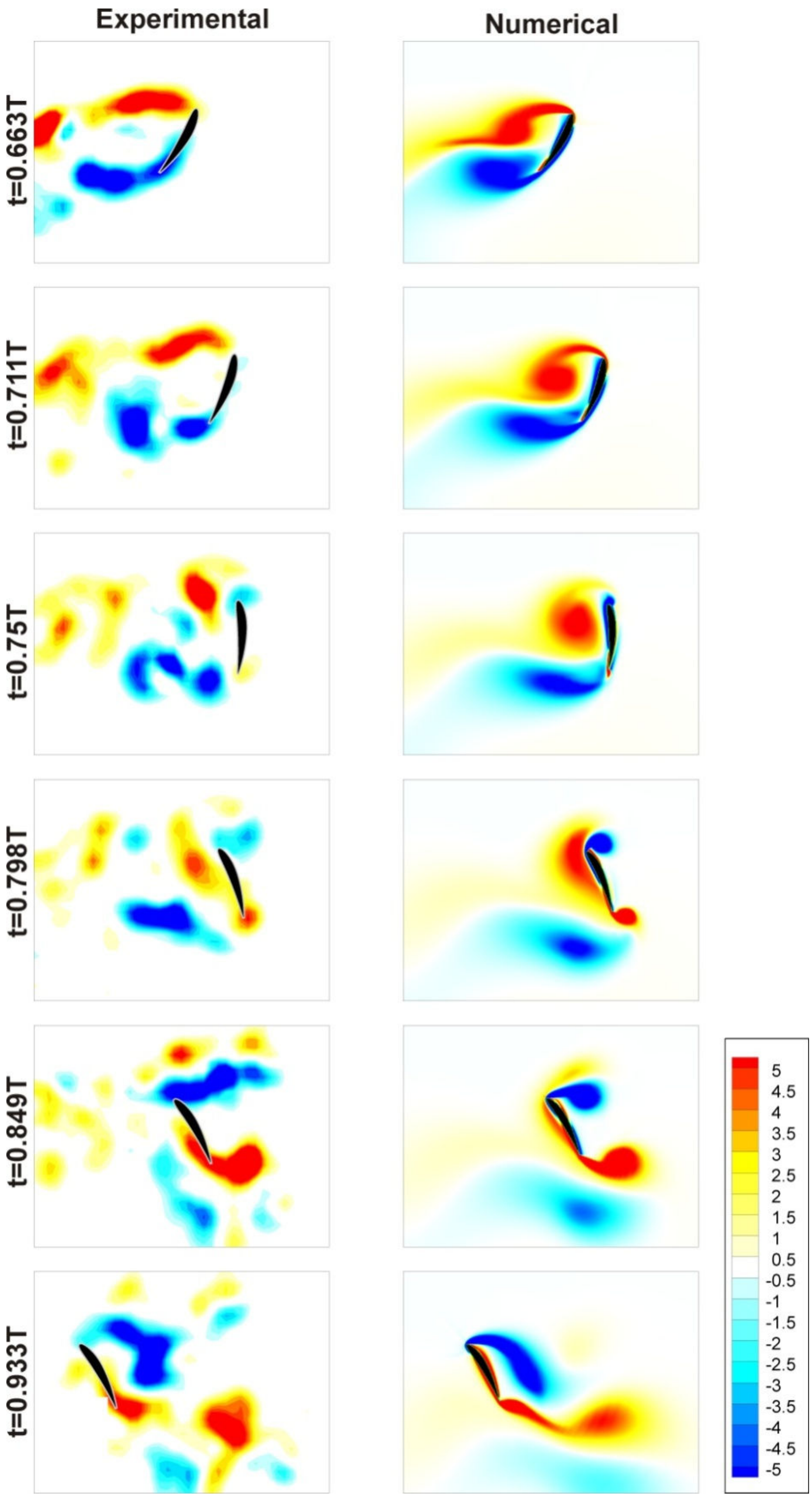

Figure A.6 Vorticity contours derived from experimental and numerical results for NACA 6412 airfoil at $\alpha_0=60^0$ (Camera 2)

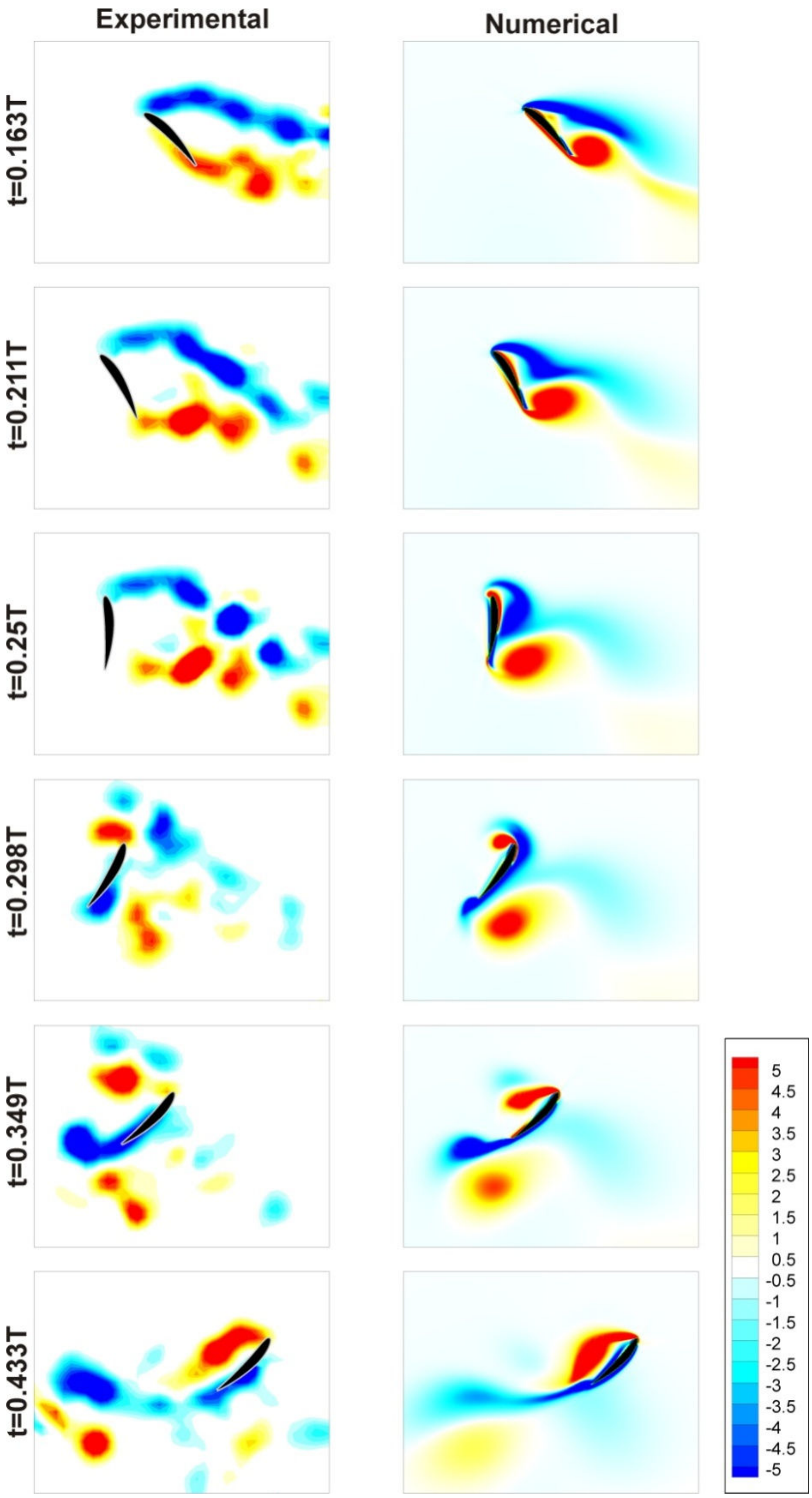

Figure A.7 Vorticity contours derived from experimental and numerical results for NACA 6412 airfoil at $\alpha_0=45^0$ (Camera 1)

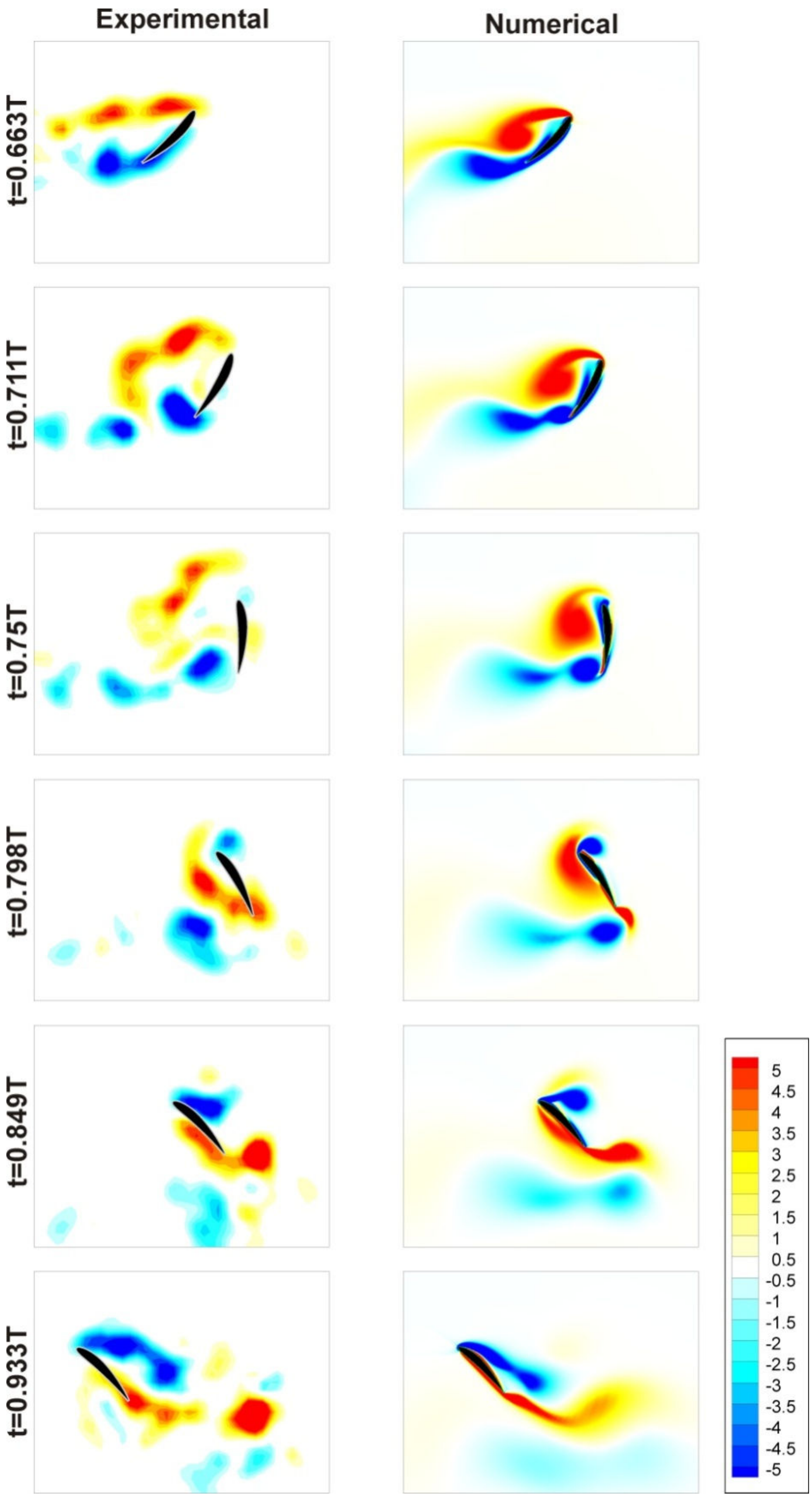

Figure A.8 Vorticity contours derived from experimental and numerical results for NACA 6412 airfoil at $\alpha_0=45^0$ (Camera 2)

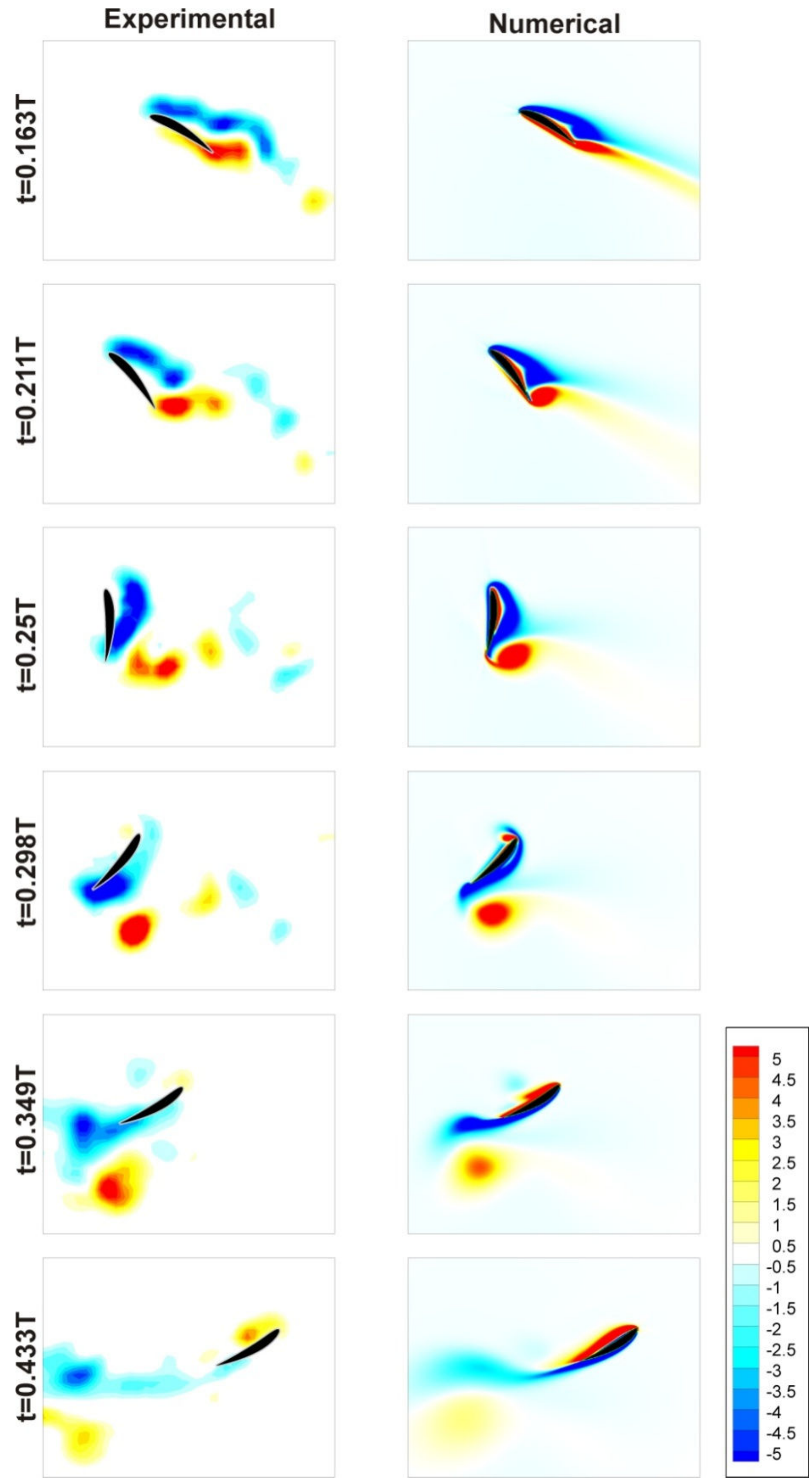

Figure A.9 Vorticity contours derived from experimental and numerical results for NACA 6412 airfoil at $\alpha_0=30^0$ (Camera 1)

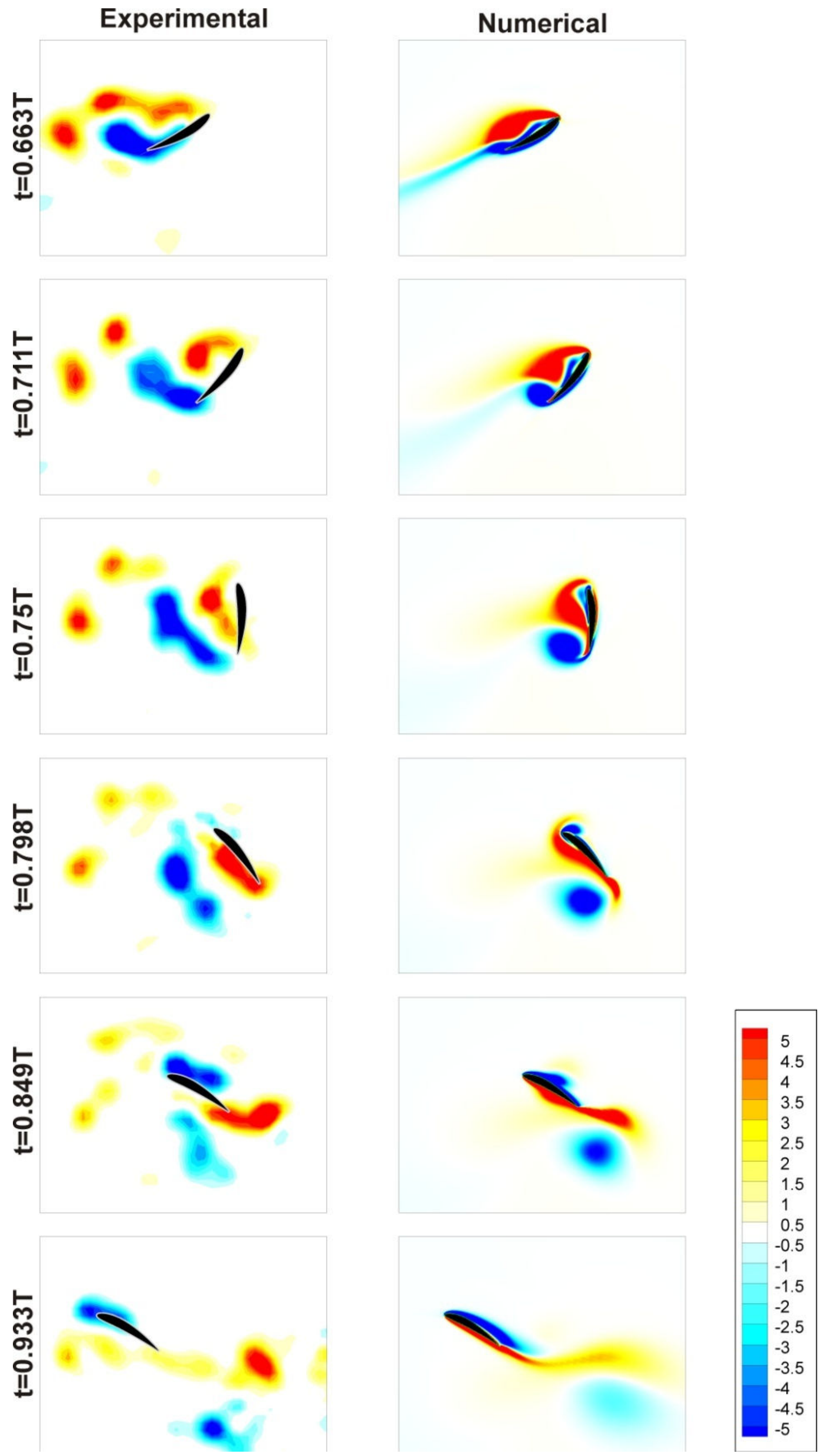

Figure A.10 Vorticity contours derived from experimental and numerical results for NACA 6412 airfoil at $\alpha_0=30^0$ (Camera 2)